Icarus **155**, 393–424 (2002)
doi:10.1006/icar.2001.6740, available online at http://www.idealibrary.com on IDEAL®

Atmospheric Chemistry in Giant Planets, Brown Dwarfs, and Low-Mass Dwarf Stars

I. Carbon, Nitrogen, and Oxygen

Katharina Lodders and Bruce Fegley, Jr.

Planetary Chemistry Laboratory, Department of Earth and Planetary Sciences, Washington University, Campus Box 1169, St. Louis, Missouri 63130-4899
E-mail: lodders@levee.wustl.edu

Received March 23, 2001; revised August 6, 2001

The chemical species containing carbon, nitrogen, and oxygen in atmospheres of giant planets, brown dwarfs (T and L dwarfs), and low-mass stars (M dwarfs) are identified as part of a comprehensive set of thermochemical equilibrium and kinetic calculations for all elements. The calculations cover a wide temperature and pressure range in the upper portions of giant planetary and T-, L-, and M-dwarf atmospheres. Emphasis is placed on the major gases CH_4, CO, NH_3, N_2, and H_2O but other less abundant gases are included. The results presented are independent of particular model atmospheres, and can be used to constrain model atmosphere temperatures and pressures from observations of different gases. The influence of metallicity on the speciation of these key elements under pressure–temperature (P–T) conditions relevant to low-mass object atmospheres is discussed. The results of the thermochemical equilibrium computations indicate that several compounds may be useful to establish temperature or pressure scales for giant planet, brown dwarf, or dwarf star atmospheres. We find that ethane and methanol abundance are useful temperature probes in giant planets and methane dwarfs such as Gl 229B, and that CO_2 can serve as a temperature probe in more massive objects. Imidogen (NH) abundances are a unique pressure-independent temperature probe for all objects. Total pressure probes for warmer brown dwarfs and M dwarfs are HCN, HCNO, and CH_2O. No temperature-independent probes for the total pressure in giant planets or T-dwarf atmospheres are identified among the more abundant C, N, and O bearing gases investigated here.

Key Words: **Jupiter; giant planets; extrasolar planets; brown dwarfs; Gliese 229B; T dwarfs; L dwarfs; M dwarfs; atmospheric chemistry; carbon; nitrogen; oxygen; methane; carbon monoxide; ammonia; thermo-chemical equilibrium.**

INTRODUCTION

The upper atmospheres of low-mass stars, brown dwarfs, and giant gas-rich planets are cool enough to allow formation of monatomic and molecular gases compared to atmospheres of stars such as the Sun. Methane (CH_4) is the most abundant carbon bearing gas in giant planet atmospheres and in brown dwarfs such as Gl 229B, while carbon monoxide (CO) is the most abundant carbon bearing gas in more massive and hotter objects such as M dwarfs, and the L dwarfs. The new group of L dwarfs consists of objects that have lower effective temperatures than M dwarfs. The L-dwarfs spectra are dominated by strengthening metal hydride bands, neutral alkali lines, and increasing depth of the water bands with decreasing temperature, but methane bands at 1.6 and 2.2 μm are absent (Kirkpartick *et al.* 1999, Martin *et al.* 1997, 1999). The cooler late-type L dwarfs ($T_{eff} < 1800$ K) begin to show the strong fundamental 3.3-μm methane absorption (Noll *et al.* 2000). Only in cooler objects do chemical changes in the atmosphere make methane dominant and the observation of methane and water absorption in the 1–2.5 micron range in Gl 229B identified it as the first bona fide brown dwarf (Nakajima *et al.* 1995, Oppenheimer *et al.* 1995). Gl 229B is the prototype of the new group of low-mass objects now called "T dwarfs" (Kirkpartick *et al.* 1999) since several similar objects to Gl 229B were discovered by the Sloan Digital Sky Survey (DENIS) and the Two Micron All Sky Survey (2MASS); see Burgasser *et al.* (1999, 2000a, 2000b), Cuby *et al.* (1999), Strauss *et al.* (1999), and Tsvetanov *et al.* (2000). In T dwarfs, methane and water bands are strong in the 1–3-μm region while the 2.3-μm CO band is absent. It was only recently that early T dwarfs bridging the transition from L dwarfs to T dwarfs were discovered, showing both methane and CO absorption bands (Leggett *et al.* 2000).

There are several motivations for this work. Spectroscopic studies to characterize substellar mass objects, i.e., T and L dwarfs, and putative extrasolar gas giant planets such as 51 Pegasi B, are highlighted as one of the two most compelling issues for scientific study by the Space Studies Board (1998). Our theoretical modeling is important for interpreting and guiding these spectroscopic studies (e.g., Geballe *et al.* 2001, Saumon *et al.* 2000). Second, theoretical models of the chemistry of the deep atmospheres of Jupiter, Saturn, Uranus, and Neptune in the 100–1000-bar region are important for the design of deep atmospheric

0019-1035/02 $35.00

entry probes to these planets (e.g., Spilker and Hubbard 1997). The continuing advances in high temperature electronics, miniaturization of analytical instruments for gas chemistry, and in a number of the required spacecraft systems have made the design of 100–1000-bar probes realistic. We note that the Venera and Vega landing probes successfully functioned for about one hour at about 740 K and 100 bars on Venus' surface. Third, studies of deep atmospheric probe missions to Jupiter, Saturn, and Uranus have been recommended by the Space Studies Board (1988, 1991) because of the importance of determining the elemental composition, dynamics, and cloud composition to levels well below the water cloud base on these planets. In the case of Uranus and Neptune, the water cloud base is at about the 100-bar level (Fegley and Prinn 1986) and probes to greater depths and higher pressures are required. Last, recent models of the internal structure of Jupiter and Saturn indicate that their interiors may not be fully convective at temperatures lower than about 4000 K (Guillot *et al.* 1994a, 1994b) and may have radiative zones between 1450 and 1900 K (Guillot 1999). However, these models do not include the alkali opacities (T. Guillot, personal communication). Thermodynamic modeling of the molecular composition of solar and near-solar composition atmospheres at high pressures and temperatures is an essential input for opacity calculations that are needed to explore possible radiative zones inside the gas giant planets.

Atmospheres of giant planets, T, L, and M dwarfs have different P–T structures and have their own characteristic distribution of the elements between atomic and molecular gases, and solid and liquid condensates. We use chemical thermodynamics and kinetics to calculate which gas species and condensates are present as a function of temperature (T), pressure (P), and elemental abundances (i.e., metallicity). We previously calculated the chemical speciation for the elements in the atmospheres of Jupiter and Saturn (Fegley and Lodders 1994). This approach yields information about the chemical probes from the deep interior of the giant planets but is restricted to these two specific objects. The approach of using individual P–T profiles is impractical for calculating the chemical composition for the numerous M, L, and T dwarfs, and extra-solar giant planets.

Instead of selecting a representative P–T profile for each object to calculate the characteristic chemical composition, we plot contour diagrams of the abundances for each compound in P–T space. This general approach to describe chemical composition as a function of T and P is more indicative of the species expected for a particular group of objects. Furthermore, any P–T profile for a specific object can be superimposed on the abundance diagrams to find its chemical composition, or vice versa, the chemical speciation can be used to constrain an object's atmospheric P–T structure.

We use solar elemental abundances (Lodders and Fegley 1998) in the computations as well as metallicities that are 0.5 dex (i.e., half a log unit) higher and lower than solar. Brown dwarfs and low-mass stars among the old disk population or in older clusters may be deficient in heavier elements (all elements heavier than H and He) relative to the Sun, while younger population objects, such as the brown dwarfs in the Pleiades, are more likely to have relative excesses of heavier elements. The metallicity of "isolated" brown dwarfs and low-mass stars is probably determined by the composition of their primordial molecular clouds from which they formed. However, there is another mechanism to increase the metallicity in objects in binary systems.

Giant planets such as Jupiter and Saturn are known to have enrichments of heavy elements relative to the Sun. These enrichments are assumed to be caused by preferential accretion of rock and ice, and incomplete gas capture of H_2 and He from the solar nebula. Such effects may apply to extrasolar giant planets, brown dwarfs, or even some low-mass stars in binary (or multiple) systems. Thus, knowing the metallicity of a primary star and that of an associated giant planet, brown dwarf, or low-mass star can help to decipher the formation and accretion history of the system.

We previously reported some results of the thermochemical calculations for C and N and the rock-forming elements Al, Ca, Cr, Fe, Mg, Si, Ti, V (Fegley and Lodders 1996) and the alkali elements (Lodders 1999a). These computations were applied to develop a relative temperature scale for low-mass dwarfs and are used to interpret results of alkali element observations in low-mass stars and brown dwarfs. Here we focus on C, N, and O because these elements are typically the next most abundant elements after H and He and their chemistry is diagnostic for P and T conditions in low-mass stars, brown dwarfs, and giant planets.

METHOD OF CALCULATION

We use the CONDOR chemical equilibrium code (Fegley and Lodders 1994), previously used successfully for modeling chemistry in the solar nebula (Lodders and Fegley 1993; Lauretta and Lodders 1997), in the atmospheres and circumstellar envelopes of cool stars (Lodders and Fegley 1995, 1997a, 1997b, 1999), in the atmosphere of Venus (Fegley *et al.* 1997), in volcanic gases on Jupiter's satellite Io (Zolotov and Fegley 1998a, 1998b), and in the atmospheres of gas giant planets and brown dwarfs (Fegley and Lodders 1994, 1996; Lodders 1999a; Lodders and Fegley 1994). The results from the CONDOR code agree with results from a Gibbs free energy minimization code that was developed by others (see Fegley *et al.* 1997; Zolotov and Fegley 1998a, 1998b) and with results from other groups using other computer codes [e.g., the METKON code described by Fegley and Palme (1985) or the code described by Barshay and Lewis (1978)]. Some results showing the versatility of the code are described on our webpage (http://solarsystem.wustl.edu).

Where relevant, we considered the possible effects of vertical mixing on the abundances of gases which are observed (e.g., CO) or possible (e.g., N_2, HCN) chemical probes of the deep atmospheres of the gas giant planets in our solar system. These calculations were done using a chemical dynamical model described elsewhere (e.g., Fegley and Prinn 1985, 1986, 1988a, 1988b; Fegley and Lodders 1994). As discussed below, we compare results from the Prinn and Barshay (1977) and Yung *et al.* (1988) kinetic schemes for CO reduction to CH_4, and show that

the latter scheme apparently does not reproduce the observed CO abundances on Jupiter and Saturn.

Thermochemical Computational Algorithm

The CONDOR code simultaneously considers the dual constraints of mass balance and chemical equilibrium. Once the temperature, pressure, and bulk composition (e.g., elemental abundances) are specified, the chemical equilibrium composition of a gaseous system is fixed. It is important to recall that thermodynamics is path independent and that the path used to arrive at a P–T point does not affect the chemical equilibrium composition. The operation of the CONDOR code is illustrated with an example based on a simplified version of the nitrogen thermochemistry.

In this example the total nitrogen elemental abundance is denoted as ΣN and it is assumed that the only important nitrogen gases are N_2 (g), NH_3 (g), HCN (g), and CH_3NH_2 (g). The mass balance expression for nitrogen, which equates the total nitrogen elemental abundance (ΣN) to the sum of the abundances of all N gases, is given by the equation

$$\Sigma N = 2P_{N_2} + P_{NH_3} + P_{HCN} + P_{CH_3NH_2}, \quad (1)$$

where P_i is the partial pressure of gas i. The mass balance equation (1) is rewritten in terms of the fugacity of molecular nitrogen (fN_2), the equilibrium constants (K_i) for forming gas i from the constituent elements in their respective reference states, and the thermodynamic activities and fugacities of other elements combined with N in the gases considered. In this example these other elements are carbon and hydrogen, so the thermodynamic activity of graphite (a_{gr}) and the fugacity of molecular hydrogen (fH_2) are used. The rewritten version of Eq. (1) is

$$\Sigma N = (f_{N_2})^{0.5}\left[2K_{N_2}(f_{N_2})^{0.5} + K_{NH_3}(f_{H_2})^{1.5} + K_{HCN} \times a_{gr}(f_{H_2})^{0.5} + K_{CH_3NH_2} \times a_{gr}(f_{H_2})^{2.5}\right]. \quad (2)$$

One equation, like Eq. (2), which contains the partial pressure terms for all gases containing the element in question is written for each element in the code. This example considers only four N-bearing gases, but the actual mass balance equations in the CONDOR code are considerably more complex. For example, the mass balance equation for nitrogen contains over one hundred gases and that for hydrogen contains several hundred different gases. Furthermore, as evident from Eq. (2), the mass balance equations are coupled and nonlinear because they contain fugacities and activities for several elements.

The solution of the mass balance equations in the CONDOR code is done by making an initial guess for the activity (or fugacity) of each element. The initial guesses can be optimized and the solution will converge within fewer steps if the major gases of each element are known, but this optimization is not essential for proper operation of the code. The CONDOR code iteratively solves the set of coupled nonlinear equations and gives the thermodynamic activity (or fugacity) for each element, the abundances of all gases in the code, and information on the quality of the solution for each element. The convergence criterion used specifies that the code reaches a solution when the calculated abundance and the input abundance for each element agree within 1 part in 100,000 or better. Here, gas composition and types of condensates are computed for temperatures from 500 to 2500 K, and total pressures from 10^{+3} to 10^{-7} bars. Temperature and log pressure step sizes in the computations are 5 or 10 K and 0.04 to 0.1 log P increments, respectively. The code currently contains ~2000 gaseous and ~1600 solid and liquid species of all naturally occurring elements, for which the chemical equilibrium composition is simultaneously evaluated at a given P and T.

Thermodynamic Data

The equilibrium constants K_i are taken from the thermodynamic database used in the Planetary Chemistry Laboratory. This has been and continues to be compiled by careful evaluation of thermodynamic data published in compilations and in the refereed literature. This careful evaluation is necessary for two reasons: (1) errors and inconsistencies exist in thermodynamic data compilations, and (2) thermodynamic data from the refereed literature need to be analyzed and evaluated before use in computations (see Stull and Prophet 1967). For example, some of the tables in the third and/or fourth editions of the JANAF Tables (Chase *et al*. 1985; Chase 1999) that are incorrect and have to be recomputed before use are those for C_2H_2, S_2O, PH, PH_3, PN, and $Mg_3P_2O_8$ solid (e.g., Heirs 1994, Zolotov and Fegley 1998a, 1998b, Lodders 1999b). Computations that are done by simply copying all the tabulated data from JANAF and/or other data sources can contain errors due to the use of incorrect thermodynamic data. This is particularly important for phosphorous chemistry because the JANAF data for PH_3, PH, PN, and $Mg_3P_2O_8$, frequently used in computations of atmospheric chemistry (e.g., Burrows and Sharp, 1999) are incorrect (Lodders 1999b).

Elemental Abundances

The calculations were done using updated solar abundances for all elements (Lodders and Fegley 1998). The continuing improvements in solar spectroscopy and analyses of chondritic meteorites have led to significant changes in solar elemental abundances from those listed in the Anders and Grevesse (1989) compilation, which were used by Fegley and Lodders (1994), where we adopted uniform enrichments for heavy elements of 2.3 (Jupiter) and 6 times solar (Saturn). Solar elemental abundances that have been revised by more than 10% since Anders and Grevesse (1989) include N (16% lower), O (12% lower), P (22% lower), and S (13% lower). This is another important difference between our work and that of other groups who use the older Anders and Grevesse (1989) compilation.

The effect of changes in metallicity was investigated for [Fe/H] = +0.5 dex and [Fe/H] = −0.5 dex. Here [Fe/H] is the standard astronomical notation for the atomic heavy element

(represented by Fe) to hydrogen ratio in a given object relative to the respective solar abundance ratios defined so that $[Fe/H] = \log(Fe/H)_{object} - \log(Fe/H)_{Sun}$. Stellar spectroscopy shows that the ratios of heavy elements (e.g., C/O, N/C, Fe/Si, etc.) remain solar for metallicities down to [Fe/H] ~ -1 and only elemental abundance ratios relative to hydrogen change from the solar ratio. Below [Fe/H] < -1 the abundance ratios of heavy elements deviate from solar abundance ratios (see, e.g., Edvardsson *et al.* (1993) for determination of stellar elemental abundances over a wide range of metallicities).

Abundances with [Fe/H] $= +0.5$ (equivalent to $\sim$3.2 times solar values) are appropriate for Jupiter, where recent *Galileo Probe* results show heavy element enrichments of about three times the solar value (e.g., Niemann *et al.*, 1998, Mahaffy *et al.* 2000). On the other hand, the brown dwarf Gl 299B likely is of subsolar metallicity. Depending on adopted gravity (g), the metallicity may range from -0.5(log g $= 4.5$, $T_{eff} = 870$ K) to [Fe/H] $= -0.1$(log g $= 5.5$, $T_{eff} = 1030$ K) and at the most likely T_{eff} of 940 K, [Fe/H] is -0.3 for log g $= 5.0$ (Saumon *et al.* 2000).

Condensate Formation

The CONDOR code takes possible liquid and solid condensates into account. This is illustrated using nitrogen chemistry as an example. Solid ammonium hydrosulfide (NH_4SH) is expected to condense in the atmospheres of gas giant planets such as Jupiter. At chemical equilibrium, the condensation of NH_4SH (solid) occurs when the thermodynamic activity of this phase becomes equal to one. The thermodynamic activity of NH_4SH (solid) is dependent only upon the bulk composition, pressure, and temperature of the system and not upon the P–T path used to arrive at a given P–T point. In other words, the NH_4SH (solid) condensation curve can be plotted as a function of pressure and temperature for each metallicity we consider. However, nucleation constraints may cause condensation of NH_4SH (and other condensates) at temperatures below the chemical equilibrium condensation temperature. We do not consider nucleation constraints here.

Once the CONDOR code finds that $a(NH_4SH)$ is equal to (or greater than) one, it computes the temperature at which the activity first reached unity, resets the thermodynamic activity of NH_4SH (solid) to unity at all lower temperatures, and adds a new term $A(NH_4SH)$ to the mass balance equations for nitrogen and sulfur which takes into account the amount of NH_4SH that is condensed. (The hydrogen abundance is so large relative to that of nitrogen and sulfur that a mass balance correction for NH_4SH condensation is very small for a solar or near solar composition gas, but this term is necessary in a very high metallicity system, such as the atmospheres of Uranus and Neptune.) The gas phase and condensation calculations are coupled, and are done simultaneously using iterative methods.

The total abundance of each condensate is limited by the least abundant element in the condensate. For example, condensation of NH_4SH from a solar or a near solar composition system such as the jovian atmosphere occurs via the net thermochemical reaction

$$NH_3\ (g) + H_2S\ (g) = NH_4SH\ (solid) \qquad (3)$$

at about 230 K in Jupiter's atmosphere. The solar atomic abundances of hydrogen, nitrogen, and sulfur are 2.82×10^{10}, 2.63×10^6, and 4.47×10^5 atoms, respectively, on the cosmochemical scale where Si $= 1.00 \times 10^6$ atoms (Lodders and Fegley 1998). Here sulfur is the least abundant element and limits the amount of NH_4SH that condenses. At 230 K on Jupiter, NH_3 and H_2S are the dominant nitrogen-bearing and sulfur-bearing gases and contain $\sim$100% of all nitrogen and $\sim$100% of all sulfur in the atmosphere. The NH_3 abundance decreases by about 17% (i.e., by the S/N atomic abundance ratio) due to the condensation of NH_4SH, but H_2S is almost completely consumed by NH_4SH condensation. The H_2S abundance at lower temperatures is very small (effectively zero) and is an exponential function of temperature because it is controlled by its vapor pressure over NH_4SH (solid). Analogous constraints control the abundances of other condensates and affect the abundances of gaseous species after condensation occurs.

There is an important difference between condensate formation in a planetary, brown dwarf, or stellar atmosphere and condensate formation in a low-gravity environment such as the solar nebula (or other protoplanetary disks). In a planetary atmosphere, condensates forming directly from the gas at high temperatures ("primary condensates") settle and form cloud layers. These primary condensates do not react with the gas at altitudes $\gg H_{cloud}$ (the cloud particle number density scale height) above the condensate clouds. These condensate clouds are out of equilibrium with the overlying atmosphere. In contrast, primary condensates in the solar nebula remain dispersed in the gas. In this environment, secondary condensates form by gas–solid reactions of the primary condensates with the surrounding gas during cooling. However, in planetary atmospheres the primary condensates are segregated by condensate cloud formation and secondary condensates cannot form.

Several sets of observations demonstrate the depletion of refractory elements via condensate cloud formation at high temperatures deep in the atmospheres of gas giant planets and brown dwarfs. The absence of silane (SiH_4) and the presence of germane (GeH_4) in the atmospheres of Jupiter and Saturn is due to depletion of refractory Si, but not of volatile Ge, by condensate formation deep in their atmospheres (Fegley and Lodders 1994). Silicon is much more abundant than germanium in a solar composition gas, which has an atomic Si/Ge ratio of $\sim$8300 (Lodders and Fegley 1998). Still, SiH_4 is not observed on either Jupiter or Saturn, and the observational upper limits are $SiH_4/H_2 \sim 1 \times 10^{-9}$ by volume (1 ppbv). For comparison, the solar Si/H_2 molar ratio is 7.09×10^{-5}, which is about 71,000 times larger than the observational upper limit on the silane abundance. In contrast, GeH_4 is observed with a GeH_4/H_2 ratio $\sim$0.7 ppbv on Jupiter and $\sim$0.4 ppbv on Saturn (Lodders and Fegley 1998). These values are close to the solar Ge/H_2 molar ratio of 8.5 ppbv and the difference arises because not all Ge in

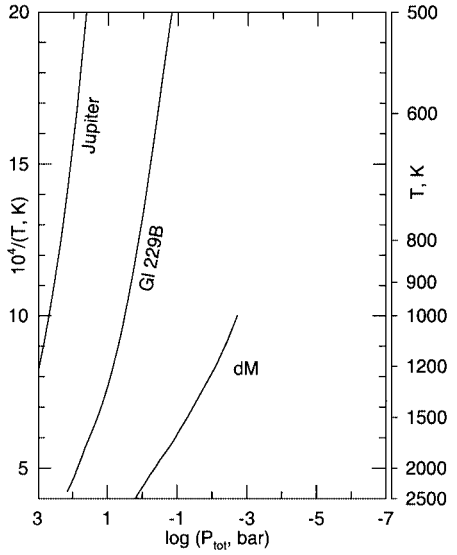

FIG. 1. Temperature–pressure profiles for Jupiter, Gliese 229B (T_{eff} = 960 K), and a M dwarf star (T_{eff} = 2200 K, dust-free). The jovian profile is an extrapolation to higher pressures and temperatures of the adiabatic P, T profile measured by the Galileo entry probe. The profiles for Gliese 229B and the M dwarf are from Marley *et al*. (1996) and Tsuji *et al*. (1996), respectively.

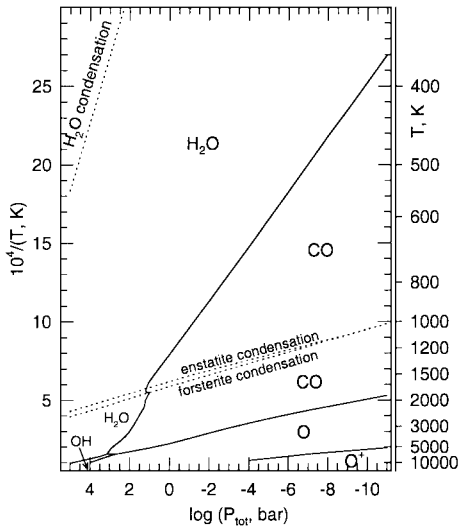

FIG. 3. The labeled regions show the presence of major oxygen bearing gases as a function of P and T for a solar composition gas. The dividing lines show where the different gases have equal abundances (e.g., CO and H_2O). The condensation temperatures of major reservoirs for condensed oxygen, i.e., water ice, enstatite, and forsterite, are indicated by dotted lines.

the atmospheres of Jupiter and Saturn is present as GeH_4 (Fegley and Lodders 1994).

The second observation is the detection by the *Galileo* entry probe mass spectrometer (GPMS) of H_2S at about three times the solar S/H_2 ratio in Jupiter's atmosphere (Niemann *et al*. 1998). The models of Lewis (1969), Barshay and Lewis (1978), and Fegley and Lodders (1994), which include depletion of Fe metal by condensate cloud formation deep in the jovian and saturnian atmospheres, predict that H_2S will be present in the jovian and saturnian tropospheres at altitudes below the NH_4SH cloud condensation level. These predictions are in agreement with the GPMS observations of H_2S on Jupiter. The *CASSINI* spacecraft will probably be able to see below the NH_4SH clouds on Saturn and should detect H_2S in the saturnian troposphere. If Fe cloud formation did not occur, H_2S would be completely absent from the atmospheres of Jupiter and Saturn because of formation of FeS (troilite) by reaction of Fe metal grains with H_2S gas at 700 K. The solar Fe/S ratio is about two and condensation of FeS consumes all H_2S gas. Thus, formation of FeS and removal of H_2S is at odds with the *Galileo Probe* observations.

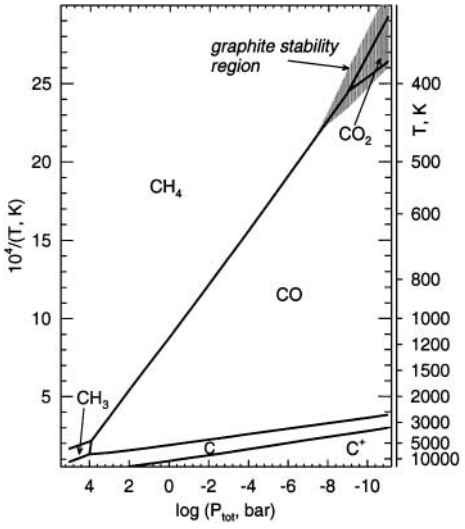

FIG. 2. The labeled regions map the presence of major carbon-bearing gases as a function of P and T in a system with solar metallicity. The dividing lines show where the different gases have equal abundances (e.g., CO and CH_4 have equal abundances on the line between their dominance fields). The shaded region at the upper right shows where elemental carbon (in the form of graphite) is thermodynamically stable.

The third observation is the detection of monatomic K gas in the atmosphere of Gliese 229B (e.g., Burrows *et al*. 2000). The calculations of Lodders (1999a) indicate that K (gas) is the dominant potassium-bearing gas until conversion to KCl (gas). The conversion of K to KCl is gradual and occurs over a wide temperature interval, but 50% of K is converted to KCl at about 1000 K and 3 bars total pressure (see Fig. 2 of Lodders 1999a). Her calculations consider the depletion of refractory rock-forming elements such as Al, Ca, and Si by condensate cloud formation deep in the atmosphere of Gl 229B. If these elements were not removed by condensate cloud formation, monatomic K vapor would be removed from the atmosphere of Gl 229B by condensation into silicate minerals such as $KAlSi_3O_8$ (orthoclase) at high temperatures and would be depleted or absent in the observable atmosphere. However, this reaction sequence yields too little monatomic K gas in Gl 229B and in the even cooler T dwarf Gl 590 D. Calculations that sequester Al, Ca, and Si into deep cloud layers (e.g., Lodders 1999a) are in better agreement with the higher observed K abundances as recently shown by Geballe *et al*. (2001) for Gl 590 D.

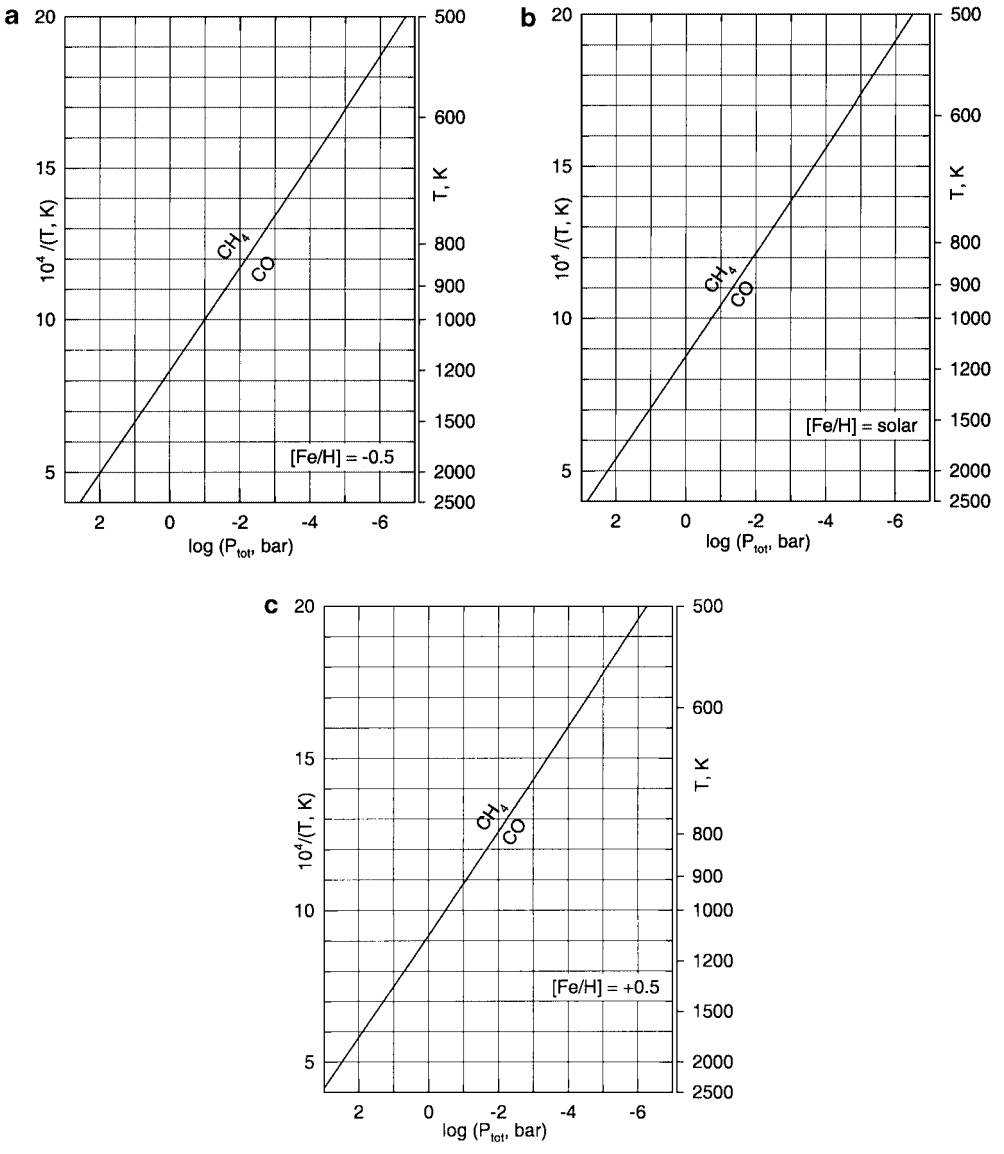

FIG. 4. The CH_4/CO boundary, along which CO and CH_4 have equal abundances, as a function of pressure and temperature for systems with a subsolar metallicity of [Fe/H] $= -0.5$ (a), solar metallicity (b), and an enhanced metallicity of [Fe/H] $= 0.5$ (c). The relative abundances of all elements heavier than He are the same as in a solar composition gas. The same three metallicities are graphed in subsequent figures.

The removal of primary condensates from the atmosphere into cloud layers is occasionally termed "rainout" and contrasted with the "no-rainout" scenario, where condensates remain dispersed in the gas (see, e.g., Burrows and Sharp (1999), Burrows *et al*. 2000). We prefer to use "condensate cloud formation" instead of "rainout" because rainout is misleading and is not the proper meteorological term. It implies that condensates are liquid, which is only the case for a limited set of condensates at high temperatures and pressures (see Lodders 1999a). If "rainout" is taken to describe settling of condensates, the term "snowing" is more appropriate. Another reason to avoid "rainout" is that rainout describes precipitation from a cloud, not precipitation into a cloud, which is what happens in brown dwarf atmospheres.

RESULTS OF THE THERMOCHEMICAL CALCULATIONS

Representative pressure, temperature profiles for the atmospheres of Jupiter, Gl 229B, and a M dwarf star (with an effective temperature of 2200 K and a dust-free atmosphere) are given in Fig. 1. The jovian profile is an extrapolation from 420 K to higher temperatures of the measured (adiabatic) profile from the *Galileo* entry probe. The profiles for Gl 229B ($T_{eff} = 960$ K) and the M dwarf star ($T_{eff} = 2200$ K) are from Marley *et al*. (1996) and Tsuji *et al*. (1996). These model atmospheres are shown to give some orientation of where different types of objects may plot in pressure–temperature space. The scales of the temperature and pressure axis are reversed so that the coolest

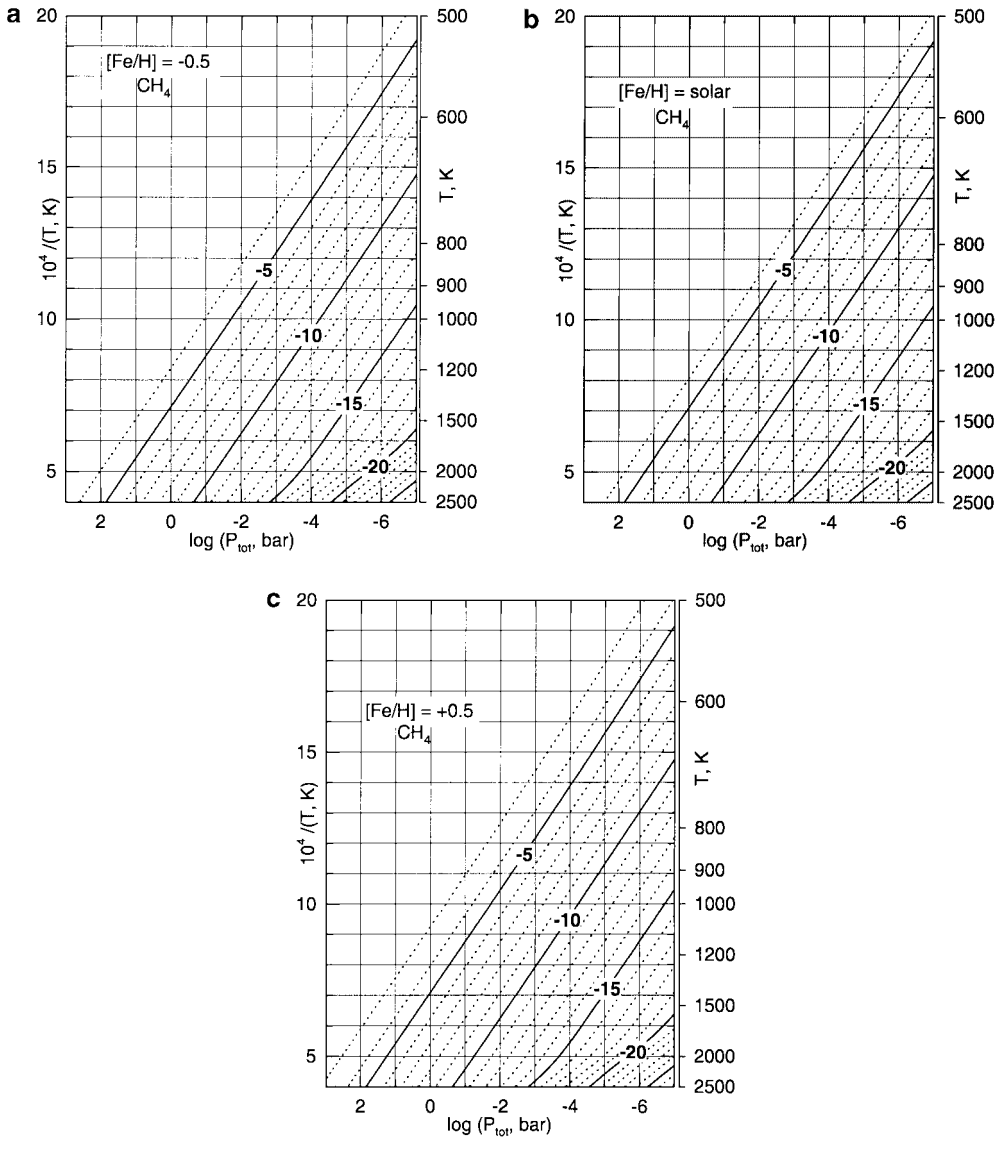

FIG. 5. Contours (on a logarithmic scale) of the methane (CH_4) mole fraction for subsolar (a), solar (b), and enhanced (c) metallicities. The methane mole fraction is defined as moles of methane divided by total number of moles of gas.

temperatures are at the top and temperatures increase downward into the atmosphere. Similarly, the pressure is lowest to the right as we move out from the interior of an object's atmosphere.

The subsequent figures illustrate our computational results for carbon, nitrogen, and oxygen chemistry. These results are *independent* of the three pressure–temperature profiles displayed in Fig. 1, and in principle can be used to constrain the pressure, temperature profiles for atmospheres of gas giant planets in our and other solar systems, brown dwarfs, and cool stars. We return to this topic when describing applications of our calculations to astronomical observations of these types of objects. We identify potential pressure and temperature probes by analyzing the chemical equilibrium abundances of compounds as a function of pressure and temperature. However, it must be remembered that chemical abundances do not directly translate to spectroscopic detectability because the latter depends on whether a compound is spectroscopically active, on transition probabilities, on line- and band strength, and on accessibility of wavelength in the observations. Many of the potential chemical probes have abundances in the ppb to ppm range that may not be detectable in objects outside the solar system. Still, the investigation of their abundances is useful because the minor species, even if not observable, may contribute to opacities in low-mass objects.

With a few exceptions, all figures are drawn to the same scale. This facilitates comparisons of chemistry with P–T profiles. We find that it is convenient to make this comparison by overlaying a transparency of Fig. 1 on the abundance contour diagrams. As discussed in many textbooks, at thermochemical equilibrium, the chemistry for a given set of elemental abundances is uniquely defined at any given P and T point without the need

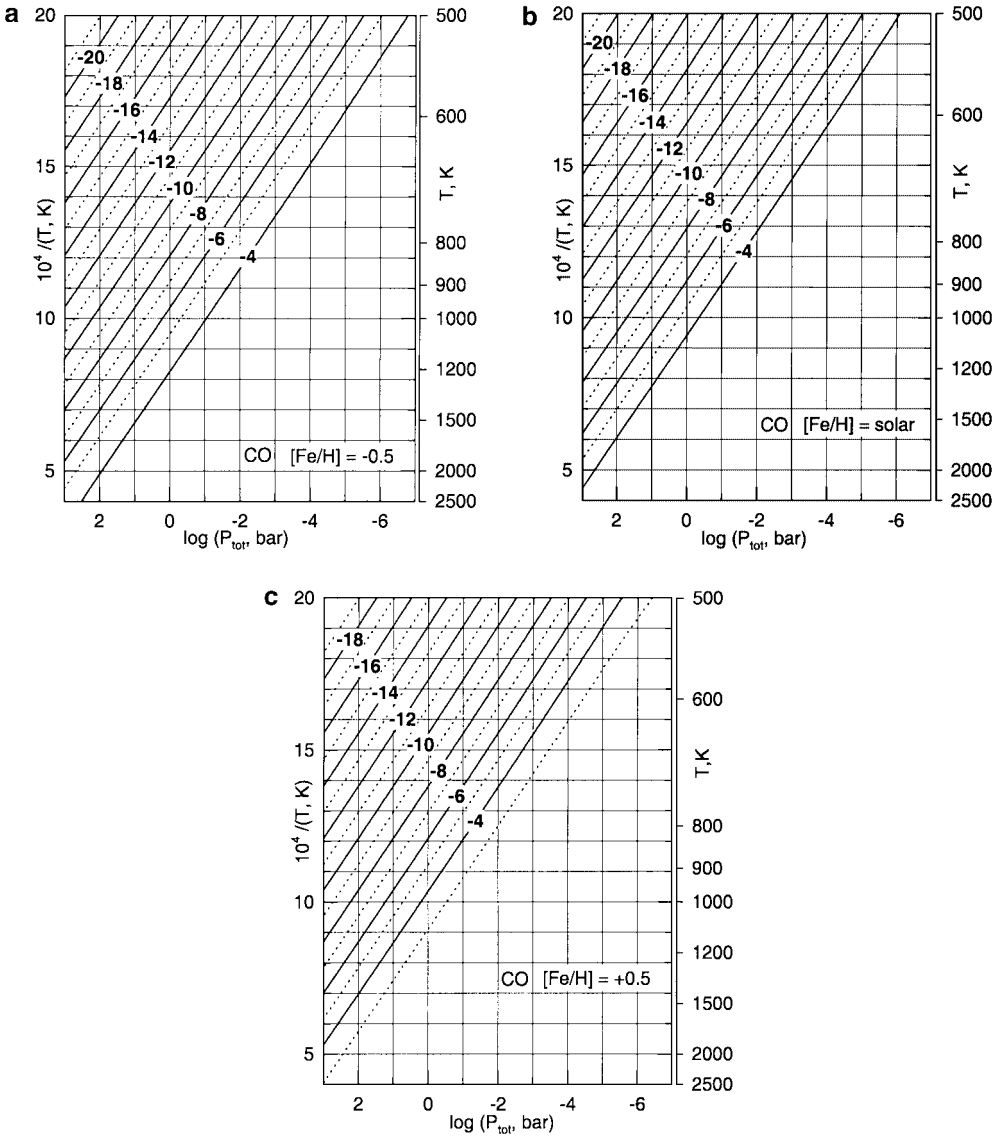

FIG. 6. Contours (on a logarithmic scale) of the carbon monoxide (CO) mole fraction for subsolar (a), solar (b), and enhanced (c) metallicities. The CO mole fraction is defined as moles of CO divided by total number of moles of gas.

for other constraints. Therefore, we can use a general approach of computing the chemistry in a wide P–T grid. If we want to look at the equilibrium chemistry of a specific object, we overlay its P–T profile on this grid. Abundances along the object's P–T profile are then obtained by reading the crossing contour lines. Similarly, whenever an object's P–T profile crosses a condensation line, it indicates the P and T where the condensate forms in the object of choice.

Carbon and Oxygen Chemistry

Dominance Fields of Major Carbon-Bearing Gases

The major carbon-bearing gases in a solar composition gas of any given metallicity are generally methane, carbon monoxide, and/or carbon dioxide, depending on temperature and total pressure. Hot and less dense atmospheres are more likely to show abundant CO (and CO_2 at lower T), while in cooler and more dense objects methane is the abundant gas. Figure 2 defines the pressure and temperature regions where different carbon gases constitute the major form of carbon in a solar metallicity atmosphere. For example, the region labeled CH_4 shows the pressures and temperatures where methane is the major carbon gas, and the region labeled CO shows the pressures and temperatures where carbon monoxide is the major carbon gas. These two gases are converted into one another by the net thermochemical reaction,

$$CO + 3H_2 = CH_4 + H_2O, \tag{4}$$

and they have equal abundances (A_i), along the line dividing these two regions [$A(CH_4) = A(CO)$]. At any point in P–T space

the abundances of these two gases do not drop to zero as this line is crossed. Methane is present (although no longer dominant) inside the region where CO is the major carbon gas, and vice versa. Except at very high temperatures, this line shows where CH_4 and CO are equivalent to about one-half of the total carbon abundance [$A(CH_4) = A(CO) \approx \frac{1}{2}\Sigma C$]. At very high temperatures, methane and CO thermally dissociate via the net thermochemical reactions

$$CH_4 = CH_3 + H \quad (5)$$

$$CO = C + O, \quad (6)$$

and the methyl radical (CH_3) and monatomic carbon vapor (C gas) become the major forms of carbon. The CH_4-CH_3-CO triple point, where the three gases have equal abundances [$A(CH_4) = A(CH_3) = A(CO)$] is at ~4695 K and ~8904 bar (the abundance of each gas equals about one third of the total carbon abundance). The CO-CH_3-C triple point [$A(CO) = A(CH_3) = A(C)$] is at ~7718 K and ~10,000 bars. At higher temperatures, monatomic carbon vapor thermally ionizes via the net reaction

$$C = C^+ + e^-, \quad (7)$$

and C^+ is the major carbon gas. The C-C^+ boundary takes thermal ionization of other elements and compounds into account because thermal ionization of the alkali metals (and other species with ionization potentials lower than that of carbon) contributes to the electron pressure in the equilibrium constant expression for reaction (7) and hence affects the position of the C/C^+ equal abundance boundary.

At equilibrium at low temperatures, CH_4 and CO react to form graphite via the net thermochemical reactions

$$CO + CH_4 = H_2O + H_2 + 2C \text{ (graphite)} \quad (8)$$

$$CO + H_2 = H_2O + C \text{ (graphite)} \quad (9)$$

$$CH_4 = 2H_2 + C \text{ (graphite)}. \quad (10)$$

The complex phase relations at low temperatures fall into three important regions: (1) the region where graphite is thermodynamically stable, but not necessarily the most abundant form of carbon, (2) the region where graphite is both stable and also the most abundant form of carbon, and (3) the region where CO_2 is the major form of carbon.

The shaded region in Fig. 2 indicates where graphite is thermodynamically stable and where the thermodynamic activity of graphite is unity. The maximum temperature and pressure for graphite formation at equilibrium in a solar metallicity gas are 463 K and $10^{-7.365}$ bar. Our calculated graphite stability field agrees with the results of Urey (1953) and Lewis *et al*. (1979) but includes the revisions in solar elemental abundances and in thermodynamic data since the earlier work was done.

The region where graphite is the major form of carbon is bounded at higher pressures by the graphite $=CH_4$ equal abundance line and at lower pressures by either the graphite $=$CO or graphite $=CO_2$ equal abundance lines. The maximum temperature and pressure at which graphite is the most abundant form of carbon (i.e., the graphite-CH_4-CO triple point) is 423.1 K and $10^{-8.505}$ bars. Two other triple points inside the graphite stability field are (1) the CO-CH_4-CO_2 triple point at 407.8 K and $10^{-9.025}$ bars where $A(CO) = A(CH_4) = A(CO_2)$ and $A(CO) \approx A(CH_4) \approx A(CO_2) \approx 1/5\Sigma C \approx \frac{1}{2}$ A(graphite); and (2) the graphite-CO-CO_2 triple point at 396.6 K and $10^{-9.754}$ bars.

The third region where CO_2 is the major form of carbon surrounds the graphite-rich region. Carbon dioxide is produced from CO and CH_4 via the net thermochemical reactions

$$CO + H_2O = CO_2 + H_2 \quad (11)$$

$$CH_4 + 2H_2O = CO_2 + 4H_2. \quad (12)$$

The net thermochemical reactions

$$2CO = CO_2 + C \text{ (graphite)} \quad (13)$$

$$2CH_4 + 2H_2O = CO_2 + 2H_2 + C \text{ (graphite)} \quad (14)$$

$$CO_2 + CH_4 = 2H_2O + 2C \text{ (graphite)}, \quad (15)$$

which form graphite are also important in this field.

Dominance Fields of Major Oxygen-Bearing Gases

Figure 3 shows the major oxygen-bearing gases as a function of T and P as done for carbon-bearing gases in Fig. 2. The major oxygen-bearing gases in a solar composition gas of any given metallicity are water and carbon monoxide, depending on temperature and total pressure. Generally, H_2O gas is the major

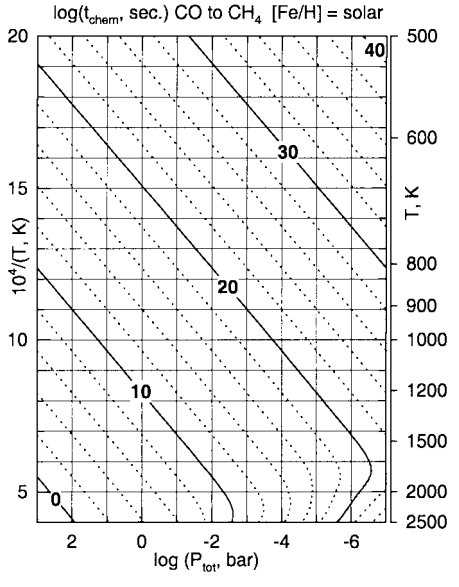

FIG. 7. Logarithmic time scale (seconds) contours for the chemical conversion of CO to CH_4. The conversion of CO to CH_4 is favored at high pressures and high temperatures.

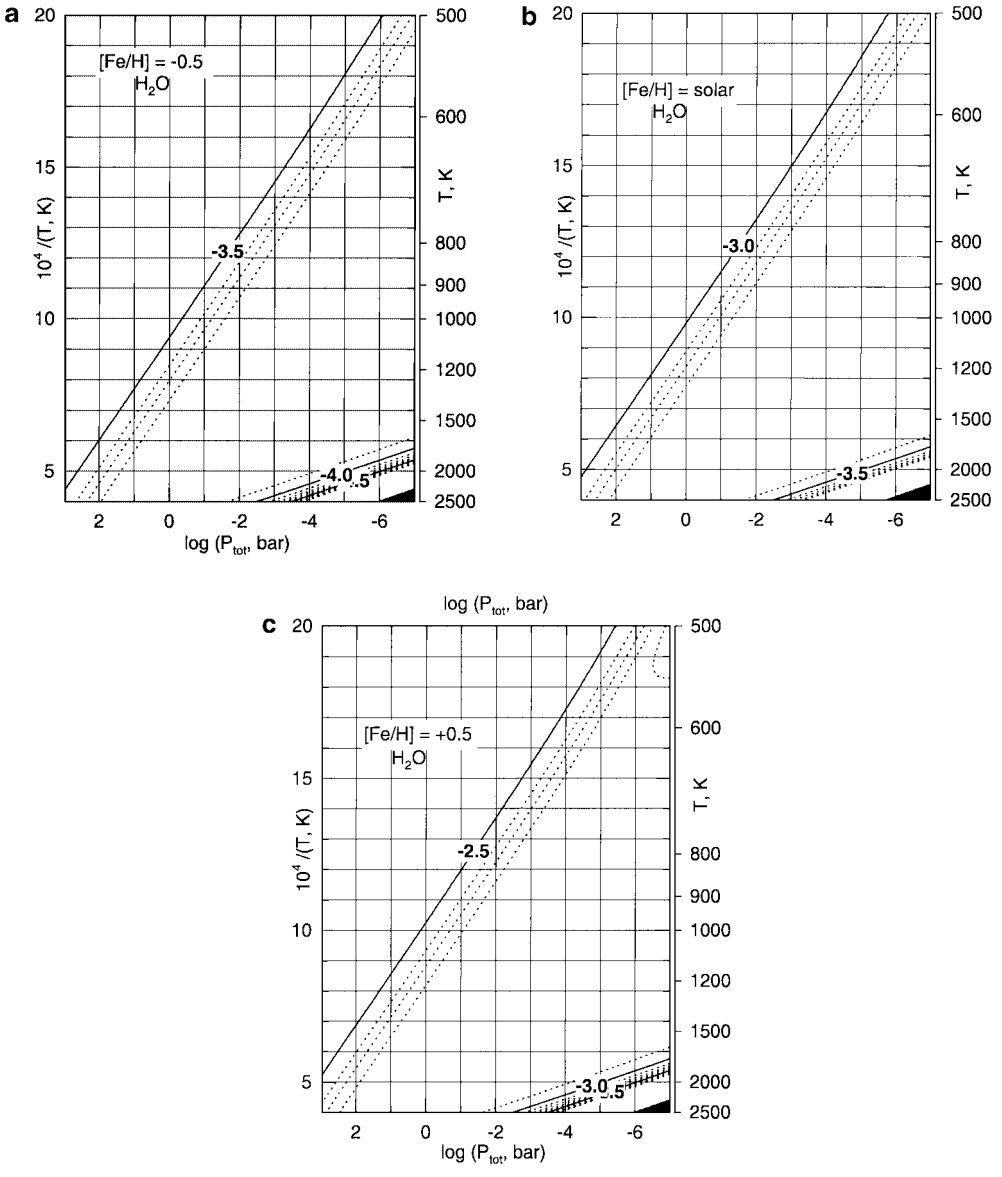

FIG. 8. Contours (on a logarithmic scale) of the water vapor (H_2O) mole fraction for subsolar (a), solar (b), and enhanced (c) metallicities.

O-bearing gas at low temperatures and high pressures, while CO gas is dominant at high temperatures and low pressures. At very high temperatures, thermal dissociation of CO to C and O gases takes place on the low pressure side while at high pressures, H_2O dissociates to OH and H.

The distribution of oxygen between H_2O and CO is affected by forsterite (Mg_2SiO_4) and enstatite ($MgSiO_3$) condensation because these major condensates provide a sink for oxygen at high temperatures. Oxygen removal from the atmosphere is limited by the abundances of Si and Mg. If all Si and Mg are condensed, only about 14.5% of all oxygen is bound into the Mg-silicates. The condensation of the less abundant Ca-, Al-, and Ti-bearing oxides at higher temperatures than forsterite only removes about 1% of total oxygen from the gas. Massive removal of oxygen from the gas only occurs when water ice (or liquid) condenses at very low temperatures (see discussion below).

A comparison of the P–T profiles in Fig. 1 with Figs. 2 and 3 shows that the regions where either CO or CH_4 are the dominant carbon gases, or H_2O and CO are the major oxygen gases, are of most interest for the atmospheres of gas giant planets, T and L dwarfs, and cool M dwarfs. Our discussion of individual gases is focused on a temperature range of 500 to 2500 K and pressures from 10^{-7} to 10^3 bars that are appropriate for these objects.

Methane, CH_4. As noted in the introduction, methane is the most abundant carbon-bearing gas in giant planet atmospheres and in brown dwarfs such as Gl 229B, while CO is the most abundant carbon-bearing gas in more massive and hotter

objects such as L and M dwarfs. Figures 4a–4c show curves of equal abundances of methane and CO defining the temperature–pressure regimes where either gas is most abundant for three different metallicities ([Fe/H] = −0.5, solar, and +0.5). The lines of equal abundances for CO and methane indicate where essentially all carbon is evenly divided between CO and CH_4 because other C-bearing gases such as CO_2 are much less abundant (see Fig. 2). The point of Figs. 4a–4c is that the CH_4 = CO boundary depends on pressure and temperature, and, as discussed below, the position of the equal abundance curves show a parallel shift towards the methane field with increasing overall metallicity.

These findings pose challenges for using the presence of methane as a temperature indicator for low-mass objects, as discussed by Lodders (1999c) and Noll *et al*. (2000). First, the curves of equal abundances for methane and CO depend on temperature and pressure, as seen from Figs. 2 and 4a–4c. Depending on how deep an observation probes into the atmosphere, a different pressure–temperature level is observed. For example, at the one-bar level, the CH_4-CO boundary is at ∼1125 K, while at the 10-bar level, it is at ∼1390 K for solar metallicity. If we take the CH_4-CO boundary as a guide, these two different maximum temperatures are implied by the observation of methane.

Second, an estimate of the temperature from the CH_4-CO boundary assumes that CH_4 is only present once the CH_4-CO boundary is reached. Even when CO is the most abundant carbon bearing gas, methane is still present in some amount. Figures 5a–5c show contours of methane mole fractions in P–T space for different metallicities. From the CH_4-CO boundary, methane abundances decrease with increasing temperature and with decreasing total pressure. If observations probe an atmospheric level close to the CH_4-CO boundary inside the CO field methane abundances may still be large enough to allow spectroscopic detection. Then temperatures are actually higher than those inferred from the assumption that the detection of methane refers to the CH_4-CO boundary. Therefore, abundances of CH_4 make a better temperature indicator than the detection of methane alone.

Third, there are shifts in the CH_4-CO boundary as a function of metallicity (Figs. 4a–4c). The CO to CH_4 conversion is favored by low metallicities and the CH_4-CO boundary shifts to higher temperatures (at constant P) as metallicity decreases. Higher metallicities have the opposite effect and the CH_4-CO boundary is located at lower temperatures (at constant P). At given temperature and pressure, more of the total carbon is chemically bound in methane in subsolar metallicity objects. Of course, the absolute methane abundances (i.e., the CH_4/H_2 ratio) are smaller in low metallicity objects than in objects with solar abundances at a given point in the P–T field where methane is the most abundant gas.

The effect of metallicity on the position of the CH_4 = CO boundary can be explained as follows. At the temperatures and pressures considered in Fig. 4, CO and CH_4 constitute 100% of the total carbon abundance (ΣC) while CO and H_2O comprise 100% of the oxygen abundance (ΣO) in the gas

$$\Sigma C = P_{CO} + P_{CH_4} \tag{16}$$

$$\Sigma O_{gas} = P_{H_2O} + P_{CO} = 0.84\Sigma O. \tag{17}$$

About 16% of the total oxygen abundance (i.e., 3.35×10^6 atoms out of the solar abundance of 2.09×10^7 atoms) is chemically bound in rock at these temperatures and pressures, which is why the oxygen abundance in the gas is less than the total oxygen abundance. The C/O atomic ratio in a solar metallicity system is ∼0.48. Stellar spectroscopy shows that this C/O ratio remains constant at the lower and higher metallicities shown in Fig. 4. Along the CH_4 = CO boundary we rewrite the mass balance equations for carbon and oxygen as

$$\Sigma C = P_{CO} + P_{CH_4} = 2P_{CO} \tag{18}$$

$$\Sigma O_{gas} = P_{H_2O} + P_{CO} = P_{H_2O} + 0.5\Sigma C$$
$$= P_{H_2O} + 0.5\,(0.48\Sigma O). \tag{19}$$

Rearranging Eq. (19) to solve for the water vapor partial pressure yields

$$P_{H_2O} = \Sigma O_{gas} - 0.24\Sigma O \cong 0.60\Sigma O. \tag{20}$$

Using Eq. (20) to substitute the equilibrium constant expression

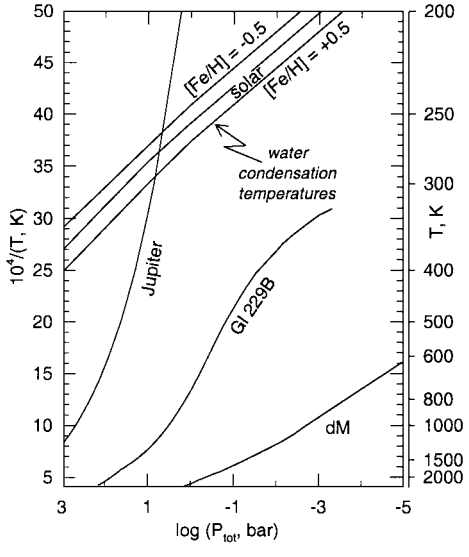

FIG. 9. Water ice and liquid water condensation temperatures for subsolar, solar, and enhanced metallicity systems. Water ice (or liquid water at and above 273.15 K) is stable on and above the condensation curves. These curves intersect the P, T profile for Jupiter, where liquid water clouds are expected, but do not intersect the P, T profiles for Gliese 229B or the M dwarf, where water ice (or liquid) clouds are not expected.

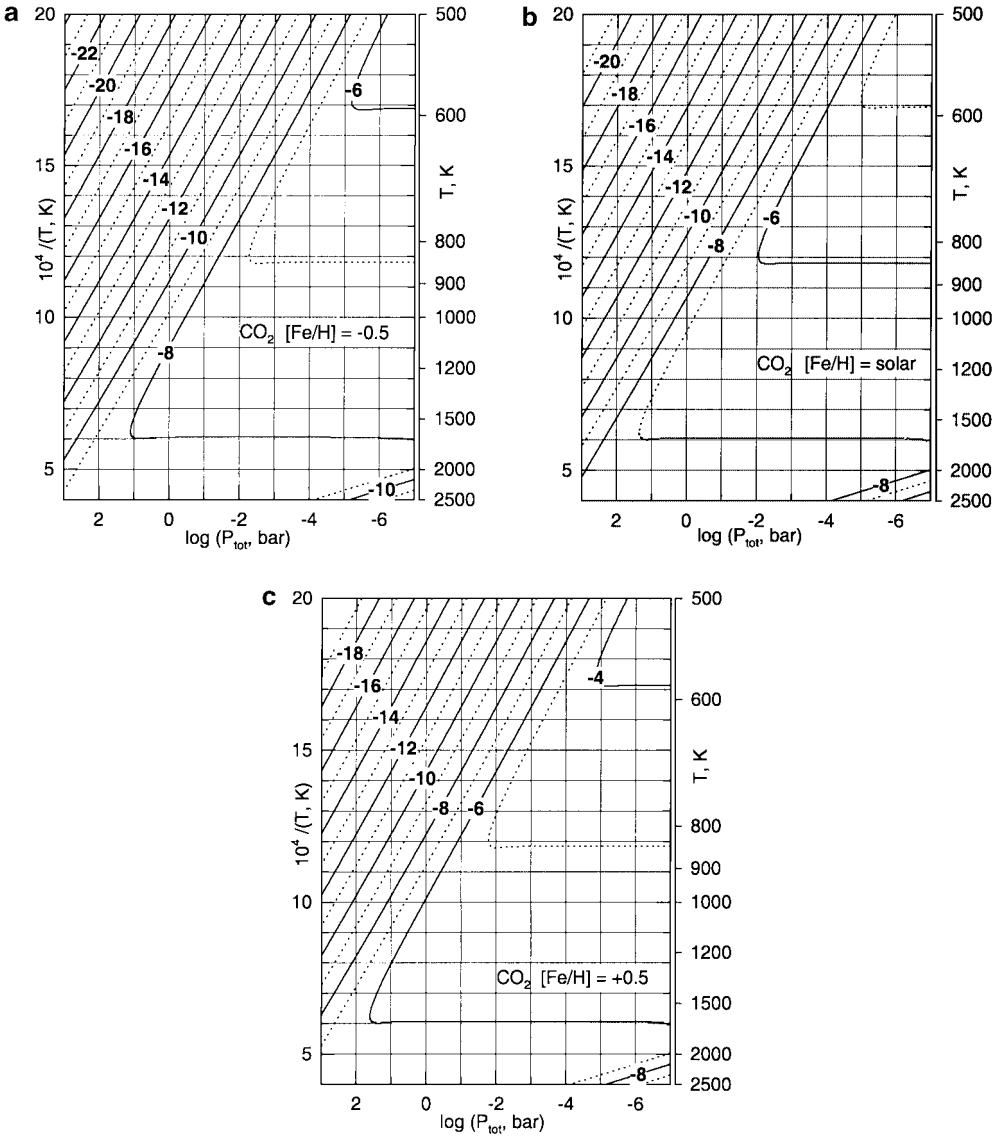

FIG. 10. Contours (on a logarithmic scale) of the carbon dioxide (CO_2) mole fraction for subsolar (a), solar (b), and enhanced (c) metallicities.

for reaction (4) gives

$$K_4 \cong P_{CH_4} P_{H_2O} / \left(P_{CO} P_{H_2}^3\right) = X_{CH_4} X_{H_2O} / \left(X_{CO} X_{H_2}^3\right) \times P_T{}^{-2} \tag{21}$$

and

$$X_{CH_4} / X_{CO} = K_4 \times P_T^2 X_{H_2}^3 / X_{H_2O} \cong K_4 \times P_T^2 X_{H_2}^3 / 0.6 X_{\Sigma O} \cong K_4 \times P_T^2 (780.83/m). \tag{22}$$

The quotient in Eq. (22) can be replaced by a constant equal to $(X_{H_2}^3/0.6X_{\Sigma O})$ in a solar metallicity system divided by a metallicity factor (m) because the H_2 mole fraction is essentially unchanged by the small metallicity variations while the water vapor mole fraction ($0.6X_{\Sigma O}$) varies linearly with the metallicity. Equation (22) shows that the CH_4/CO ratio is inversely proportional to metallicity, so as metallicity decreases, the CH_4/CO ratio at a given pressure and temperature increases, and the CH_4-CO boundary (where $CH_4/CO = 1$) moves to higher temperature.

As mentioned earlier, methane is still present inside the CO field; its abundance does not drop to zero as the CH_4-CO boundary is crossed. Methane mole fractions inside the CO field are plotted in Figs. 5a–5c. The abundance contours for CH_4 mole fractions $\leq 10^{-5}$ plot at the same pressures and temperatures for all metallicities but contours for CH_4 mole fraction $> 10^{-5}$ depend on metallicity. Note that in a solar metallicity system, a CH_4 mole fraction of 10^{-5} corresponds to a CH_4/CO ratio of $\sim$3.4%, which is equivalent to a $CH_4/\Sigma C$ ratio of $\sim$1.7%.

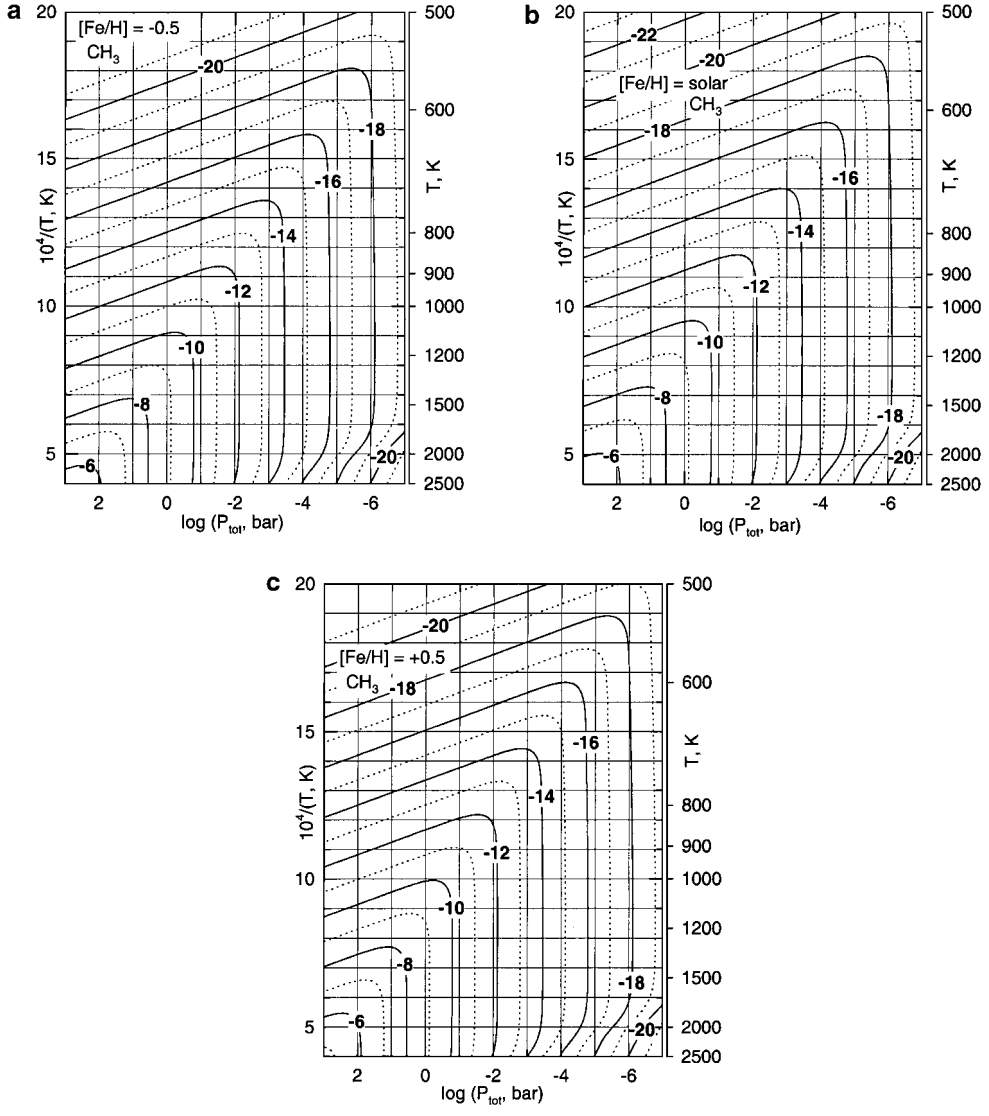

FIG. 11. Contours (on a logarithmic scale) of the methyl radical (CH_3) mole fraction for subsolar (a), solar (b), and enhanced (c) metallicities.

The abundance of CH_4 is independent of metallicity inside the CO field. Rearranging Eq. (21) to solve for the CH_4 mole fraction yields

$$X_{CH_4} = X_{CO} \cdot K_4 \cdot P_T^2 \left(X_{H_2}^3 / X_{H_2O}\right). \tag{23}$$

Inside the CO field, CH_4 is a minor part of the total carbon abundance and we rewrite the carbon mass balance equation (16) as

$$\Sigma C \cong P_{CO}, \tag{24}$$

and to a good first approximation the CO mole fraction is then given by

$$X_{CO} \cong X_{\Sigma C}. \tag{25}$$

Likewise, the H_2O mole fraction can be written as

$$X_{H_2O} \cong X_{\Sigma O_{gas}} - X_{\Sigma C}, \tag{26}$$

using Eq. (17) for the oxygen mass balance. Rewriting Eq. (23) using Eqs. (25) and (26) for the CO and H_2O mole fractions, respectively, gives

$$X_{CH_4} \cong K_4 \cdot P_T^2 \, X_{H_2}^3 \left[X_{\Sigma C} / \left(X_{\Sigma O_{gas}} - X_{\Sigma C}\right)\right] \tag{27}$$

for the CH_4 mole fraction inside the CO field for a solar metallicity system. Equation (27) is generalized to other metallicities by multiplying the solar carbon and oxygen abundances by the metallicity factor m, which is unity for a solar gas, $10^{0.5}$ for

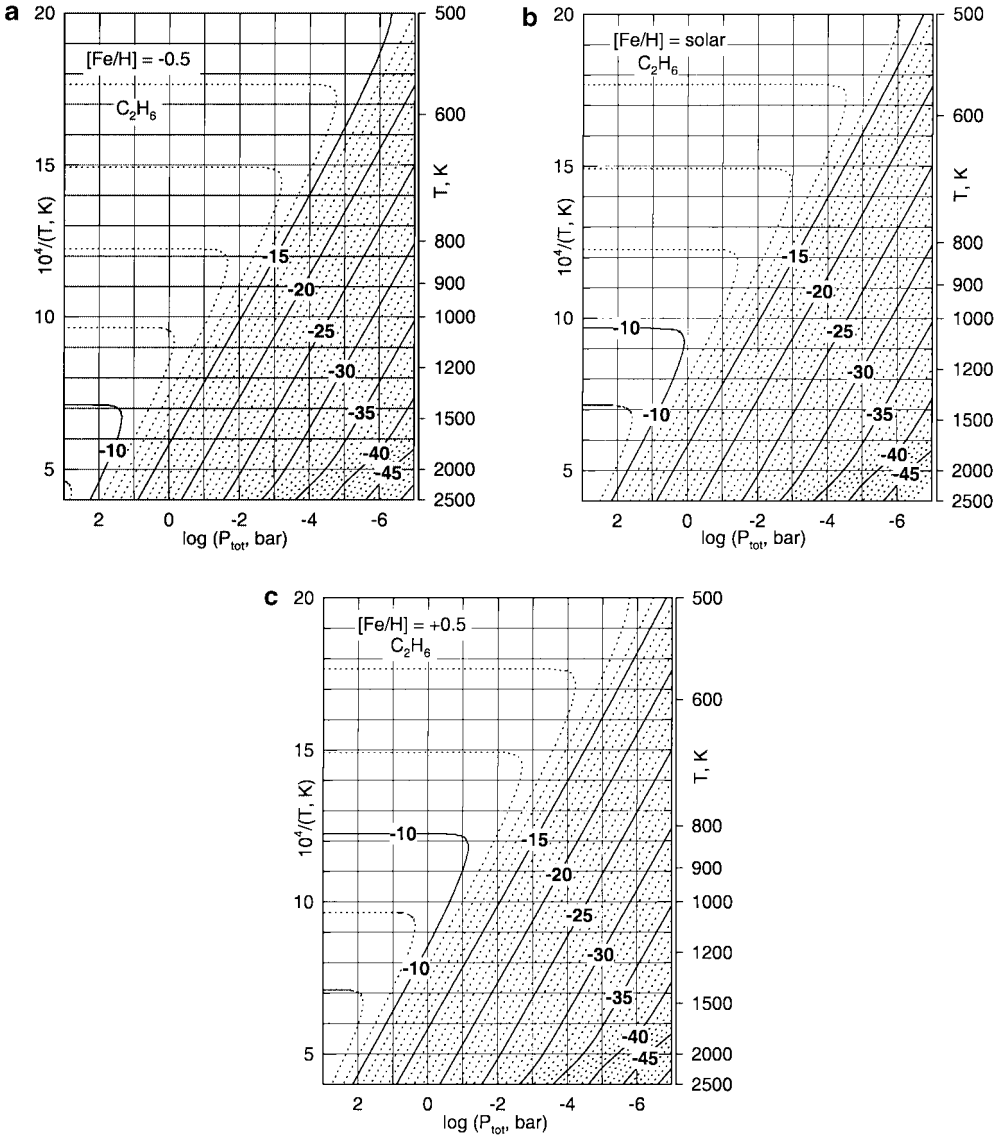

FIG. 12. Contours (on a logarithmic scale) of the ethane (C_2H_6) mole fraction for subsolar (a), solar (b), and enhanced (c) metallicities.

[Fe/H] = 0.5, and so on. We obtain the equation

$$X_{CH_4} \cong K_4 \cdot P_T^2 X_{H_2}^3 \left[m X_{\Sigma C} / \left(m X_{\Sigma O_{gas}} - m X_{\Sigma C} \right) \right]$$
$$\cong K_4 \cdot P_T^2 X_{H_2}^3 \left[X_{\Sigma C} / \left(X_{\Sigma O_{gas}} - X_{\Sigma C} \right) \right]. \quad (28)$$

The metallicity factor m cancels out of the quotient in Eq. (28) and the CH_4 mole fraction at constant pressure and temperature is the same in subsolar, solar, and supersolar metallicity systems as long as CO is the dominant carbon gas.

Equation (28) and the contours plotted in Figs. 5a–5c show that the CH_4 abundance is a potential temperature indicator in objects with CO-rich atmospheres. However, qualitative detection of CH_4 without quantitative abundance determination is a rather poor temperature indicator. If CH_4 is the major carbon gas, an upper limit for the temperature may be estimated from the $CH_4 = CO$ boundary if the metallicity is known. Only determination of the methane and the CO abundances gives information about the total carbon abundances ($\Sigma C = CO + CH_4$) and hence metallicity.

Carbon monoxide, CO. Figures 6a–6c are the counterparts to Figs. 5a–5c and show CO mole fractions inside the CH_4 field as a function of temperature, pressure, and metallicity. As discussed earlier in connection with the CH_4/CO boundary, the CO abundance decreases with decreasing temperature and increasing pressure. A comparison of the three plots in Fig. 6 shows that the CO abundance inside the CH_4 field varies with metallicity. This behavior is understood by rearranging Eq. (21) to solve for the CO mole fraction

$$X_{CO} = K_4^{-1} P_T^{-2} X_{CH_4} \cdot X_{H_2O} / X_{H_2}^3. \quad (29)$$

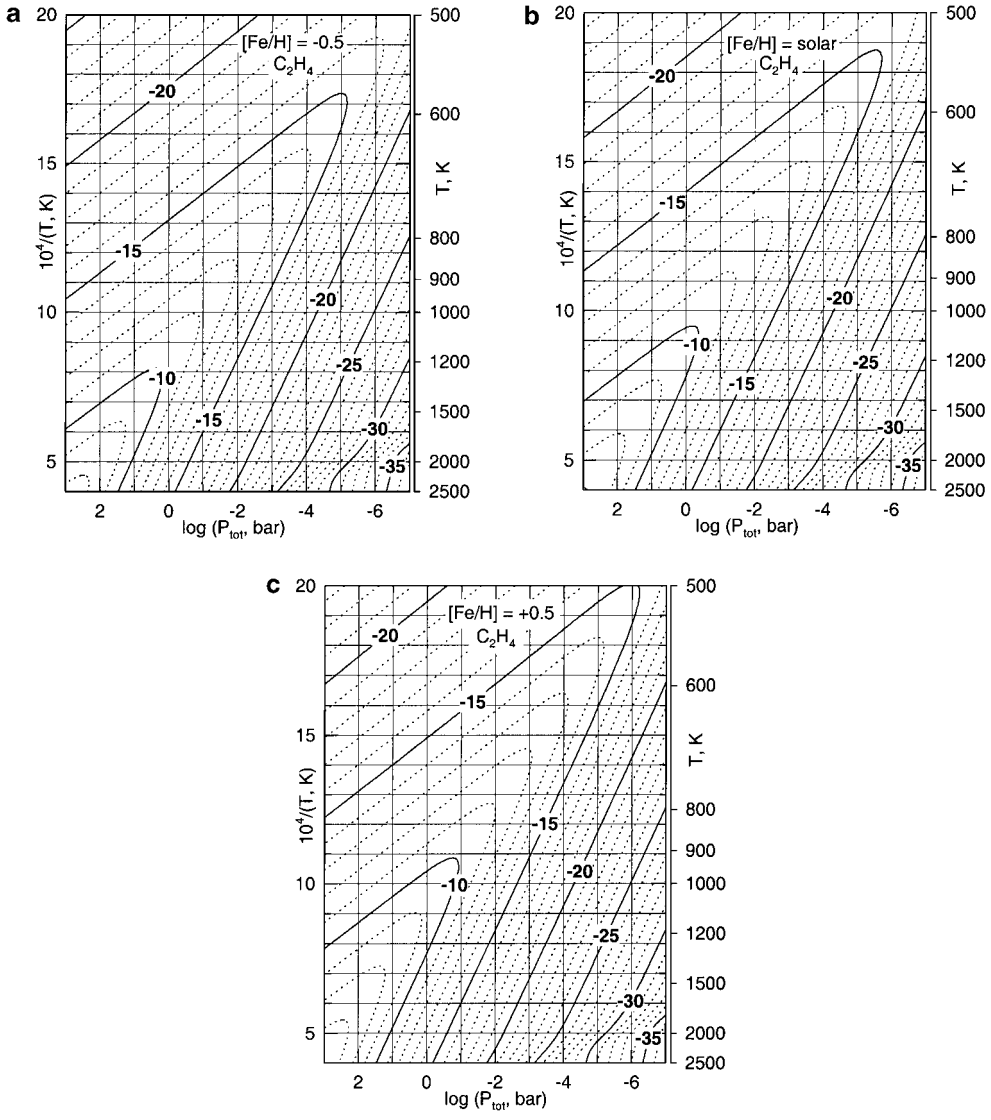

FIG. 13. Contours (on a logarithmic scale) of the ethylene (C_2H_4) mole fraction for subsolar (a), solar (b), and enhanced (c) metallicities.

Inside the CH_4 field, where the total carbon abundance can be approximated by the CH_4 partial pressure, CO comprises a minor fraction of total carbon. We rewrite the carbon mass balance equation (16) as

$$\Sigma C \cong P_{CH_4}, \tag{30}$$

and the CH_4 mole fraction is

$$X_{CH_4} \cong X_{\Sigma C}. \tag{31}$$

Because CO is negligible throughout most of the CH_4 field, H_2O comprises ~100% of the total oxygen in the gas, and the H_2O mole fraction is

$$X_{H_2O} \cong X_{\Sigma O_{gas}} = 0.84\, X_{\Sigma O}. \tag{32}$$

Substituting Eqs. (31) and (32) into Eq. (29) and again using the metallicity factor m to denote enrichments or depletions relative to solar metallicity, X_{CO} is given by

$$\begin{aligned} X_{CO} &\cong 0.84\, m^2 X_{\Sigma C} X_{\Sigma O} K_4^{-1} \cdot P_T^{-2} X_{H_2}^{-3} \\ &= 1.45\, m^2 X_{\Sigma C} X_{\Sigma O} K_4^{-1} \cdot P_T^{-2}. \end{aligned} \tag{33}$$

In the right-hand side of Eq. (33) the H_2 mole fraction of 0.833 in a solar metallicity system is taken as constant, which is a very good approximation for the small metallicity variations considered here. Equation (33) shows that inside the CH_4 field, equilibrium CO mole fractions are proportional to m^2 and have a strong dependence upon metallicity.

CO Chemical Reaction Time Scales

Figure 7 shows the chemical time scales for the CO to CH_4 conversion ($\log t_{chem}$ in seconds) as a function of temperature and pressure. The conversion is fastest at high pressures and

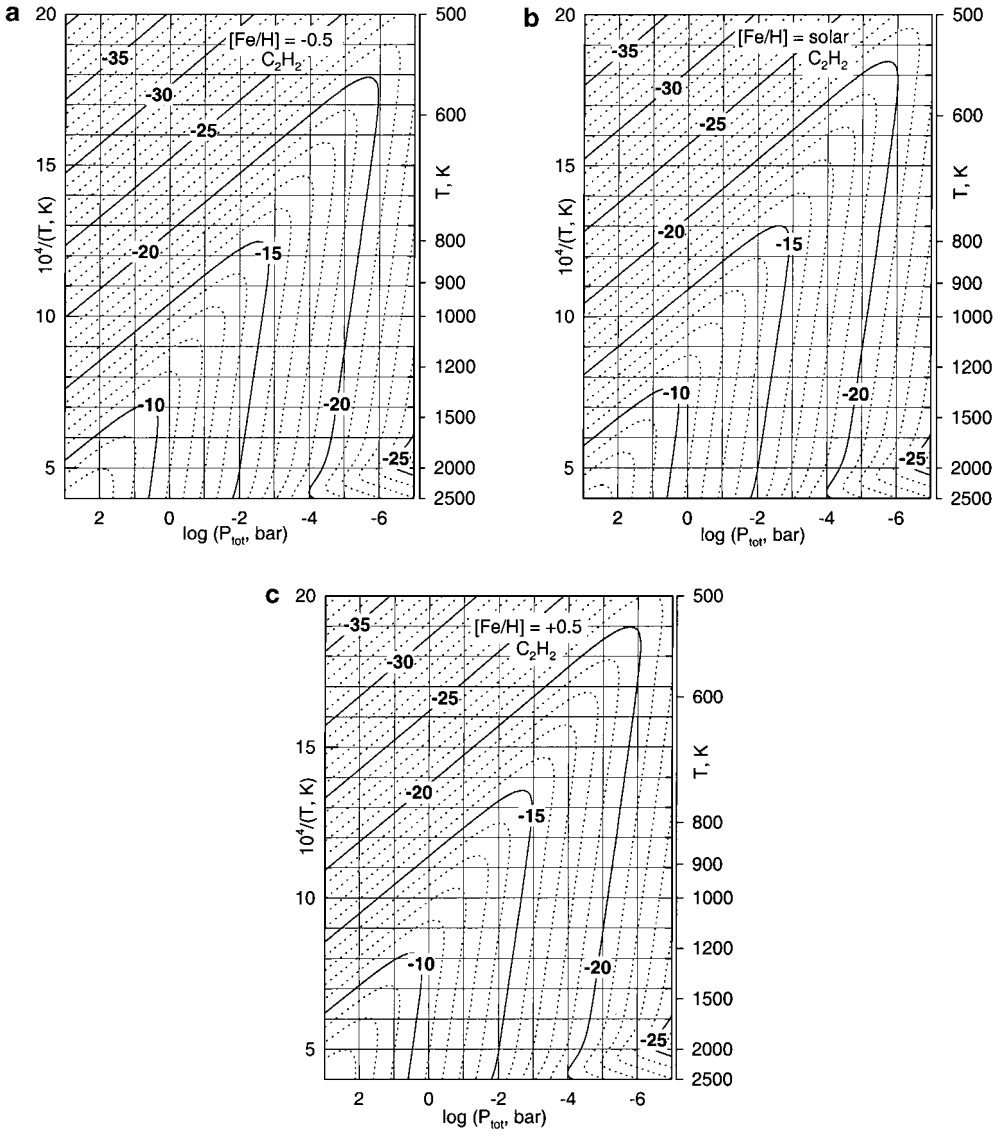

FIG. 14. Contours (on a logarithmic scale) of the acetylene (C_2H_2) mole fraction for subsolar (a), solar (b), and enhanced (c) metallicities.

temperatures, but is very slow at low temperatures and low pressures. The details for the calculation of these reaction time scales are based on the model by Prinn and Barshay (1977) and are given in Fegley and Lodders (1994). We adopted this kinetic scheme here because the results well reproduce the observed CO abundances for Jupiter and Saturn.

Carbon monoxide is observed in the upper atmospheres of Jupiter and Saturn at ∼1 part per billion by volume, and in the upper atmosphere of Neptune at ∼0.65 part per million by volume (Tables 8.3, 9.7, and 11.3 in Lodders and Fegley 1998). As first shown by Prinn and Barshay (1977), the observed CO abundances are many orders of magnitude higher than its chemical equilibrium abundance at the observed level. The presence of CO in the upper atmospheres of Jupiter, Saturn, and Neptune is probably due to rapid vertical mixing from the deep atmospheres where the equilibrium abundances of CO is much larger (Prinn and Barshay 1977; Fegley and Prinn 1985; Fegley and Lodders 1994; Lodders and Fegley 1994). In essence, CO-bearing gas parcels are convectively mixed upward at a rate that is rapid enough to quench the chemical destruction of CO in the gas parcels. The atmospheric level at which destruction of CO stops is called the quench level. The temperature and pressure of the quench level depend upon the rate of convective mixing, which is parameterized using a vertical eddy diffusion coefficient (K_{eddy}), and upon the kinetics of CO destruction. The K_{eddy} values are estimated from free convection theory and the observed heat fluxes. The kinetics of CO destruction is modeled using the scheme proposed by Prinn and Barshay (1977) in which the rate-determining step is $H_2CO + H_2 \rightarrow CH_3 + OH$, with a rate constant estimated from the rate of the reverse reaction ($CH_3 + OH$) and the equilibrium constant. The observed CO abundances on Jupiter, Saturn, and Neptune can be matched

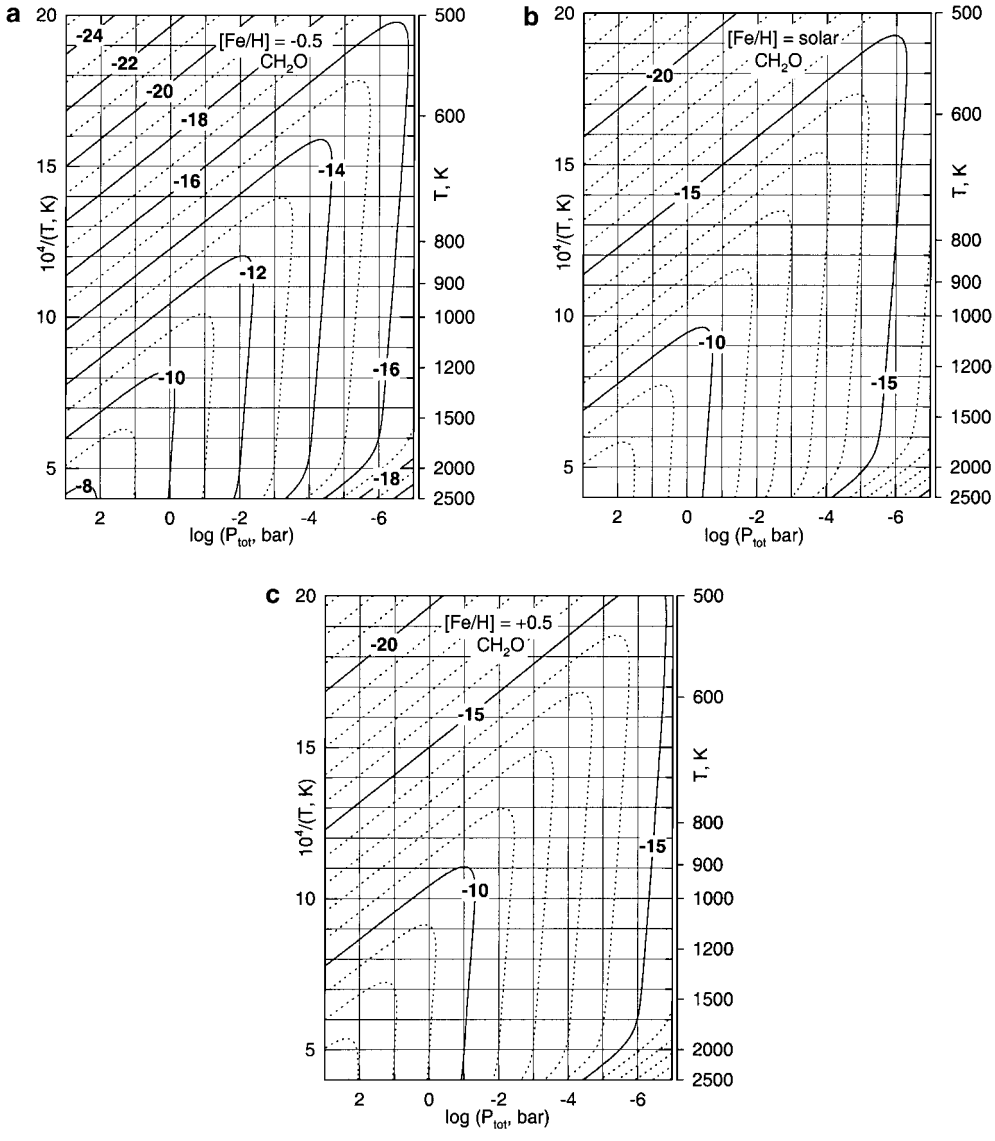

FIG. 15. Contours (on a logarithmic scale) of the formaldehyde (CH_2O) mole fraction for subsolar (a), solar (b), and enhanced (c) metallicities.

using the Prinn–Barshay thermochemical kinetic scheme. About 10 years after their scheme was proposed, Yung *et al*. (1988) suggested an alternative kinetic scheme for CO destruction that involves the methoxy radical (CH_3O), which is an important intermediate in combustion and flame chemistry. However, the Yung *et al*. model apparently did not reproduce the observed CO abundances, possibly because of incomplete experimental data on all reaction rate constants. It is also possible that chemical pathways in the high-pressure, H_2-rich atmospheres of the gas giant planets are different than those in lower pressure flames on Earth.

Shortly after Gl 229B was discovered, we made the first thermochemical equilibrium model of its atmospheric chemistry (Fegley and Lodders 1996). We used the Marley *et al*. (1996) P–T profile and showed that CO was less abundant than CH_4 at atmospheric levels cooler than 1470 K. These results led us to state: "Sufficiently rapid vertical mixing in the atmosphere of Gl 229B is expected to yield detectable quantities of CO in the atmosphere of this brown dwarf." We also suggested if CO destruction were quenched at the same temperature as on Jupiter, a CO abundance of about 10 ppmv would result. Quenching at higher temperatures would lead to more CO, while quenching at lower temperatures would lead to less CO. Subsequently, Noll *et al*. (1997) detected CO in Gl 229B and estimated its abundance at >50 ppmv, which corresponds to thermochemical equilibrium at temperatures ≥ 1250 K according to our modeling. Noll *et al*.'s observations probed a cooler atmospheric level. They proposed that the CO they saw was due to vertical transport, but they did not model this process in any detail.

More recently, Griffith and Yelle (1999) reconsidered the abundance and origin of CO in Gl 229B. They took theoretical computations of reaction rates from the literature and used

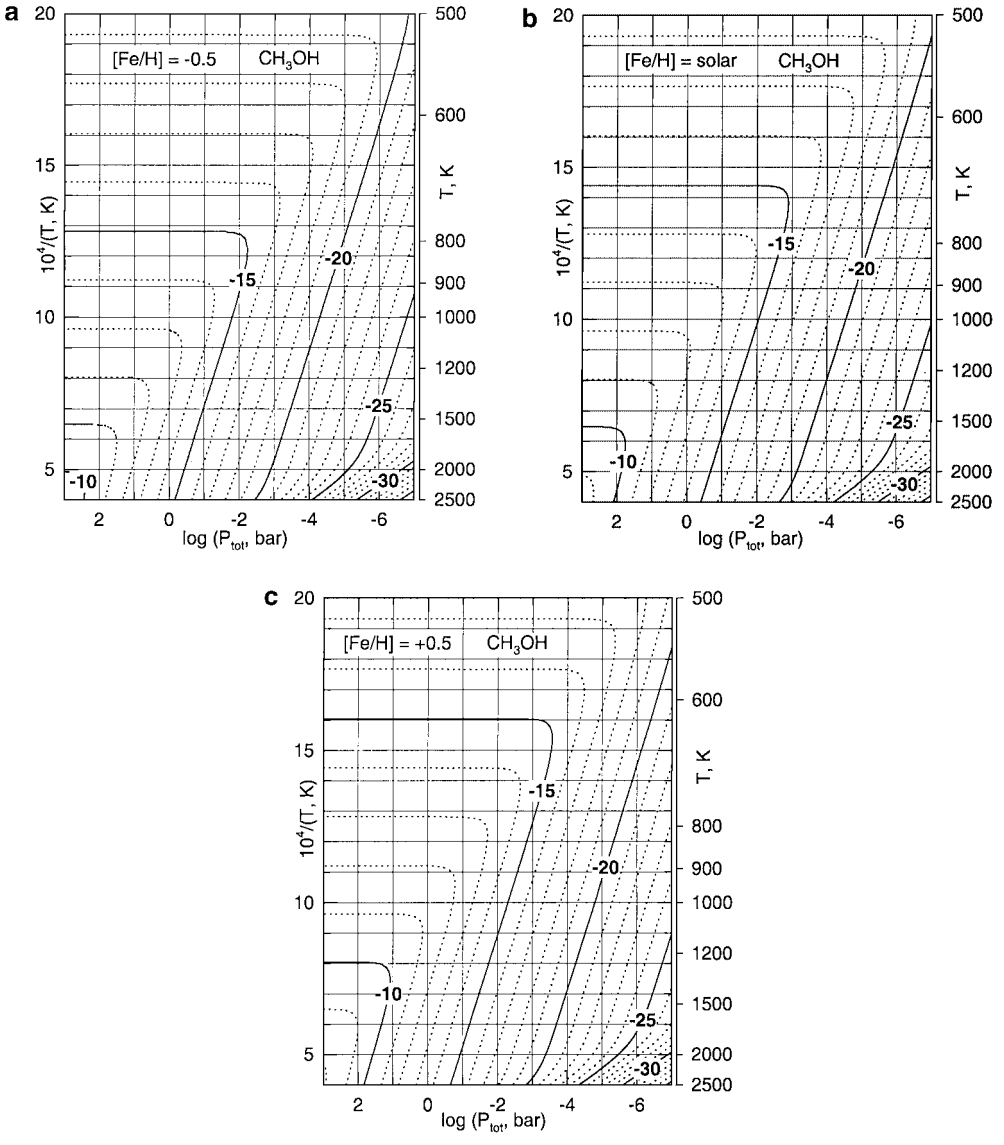

FIG. 16. Contours (on a logarithmic scale) of the methanol (CH_3OH) mole fraction for subsolar (a), solar (b), and enhanced (c) metallicities.

them to argue against the Prinn–Barshay scheme. Then they used the Yung *et al*. (1988) kinetic scheme, updated with new kinetic data, to explain the observed CO abundance on Gl 229B.

All of this stimulated our interest in taking another look at the question of how CO is reduced to CH_4 and we convinced ourselves that enough progress in combustion and flame chemistry had been made since Prinn and Barshay (1977) to address this problem (e.g., see Gardiner 2000). We plan to reexamine both the Prinn–Barshay and Yung *et al*. (1988) kinetic schemes using the newly available kinetic data to see if either, neither, or both can explain the observed CO abundances on the gas giant planets. Preliminary results for Jupiter using updated Yung *et al*. (1988) kinetics indicate that the CO abundances at the quench level are about two orders of magnitudes lower at a given K_{eddy} than those obtained from the Prinn and Barashay (1977) scheme, which reproduces observed CO abundances on Jupiter.

Here chemical lifetimes of CO, N_2, and HCN are calculated for solar metallicity. As noted by Fegley and Prinn (1985), these t_{chem} values are independent of the enrichment or depletion of heavy elements relative to solar abundances. Thus, the graphs showing log t_{chem} for CO, N_2, and HCN apply to all three metallicities we study.

Water, H_2O. Water vapor is an important opacity source in atmospheres of brown dwarfs and giant planets, especially if no water condensation has taken place. Water vapor is generally important because oxygen is about twice as abundant as carbon and even if CO is the major C-bearing gas, about half of all gaseous oxygen can be tied up in water. Carbon dioxide becomes an important C-bearing gas at very low temperatures and pressures (see Fig. 2) and the H_2O abundance is decreased inside the field of CO_2 dominance. Conversely, when methane

TABLE I
Major Carbon-, Oxygen-, and Nitrogen-Bearing Gases in Order of Decreasing Abundance at 1000 K

1000 bar	1 bar	10^{-7} bar
Carbon- and oxygen-bearing compounds		
H_2O		
CH_4	CH_4	CO
CO, C_2H_6	CO	CO_2
CH_3, CH_3OH	CO_2	CH_4
C_2H_4, CO_2, CH_2O	CH_3, C_2H_4, CH_2O, C_2H_6	CHO, CH_2O
C_3H_8, HCOOH	CH_3OH	CH_3, HCOOH
Nitrogen-bearing compounds		
NH_3	N_2	N_2
N_2	NH_3	NH_3
CH_3NH_2	HCN	HCN, NS
NH_2, HCN	HNC	HNC, NH_2, NO
HNC	CH_3NH_2, HNCO, NH_2	HCNO

becomes the major C-bearing gas, the oxygen previously tied up in CO is converted into water according to Eq. (4).

Figures 8a–8c show the water mole fractions as a function of P, T, and metallicity. Water is the major oxygen-bearing gas at temperatures below the $CH_4 = CO$ boundary (Figs. 2 and 4) and water abundances decrease at higher temperatures and lower pressures in the CO field. At a given temperature and pressure, water abundances are higher at higher metallicities because of higher O/H ratios relative to solar. Within the region of the CO field is a larger region where water abundances are relatively constant. This region of relatively constant mole fractions at high temperatures and low pressures is seen at all metallicities and occurs once CH_4 is $\leq 1\%$ of total carbon. The CO/H_2O ratio and the H_2O mole fractions are then constant over a wide P–T range. The H_2O mole fraction decreases and the CO/H_2O ratio increases at high temperatures where thermal dissociation of H_2O becomes important.

Water condensation takes place in the upper atmospheric regions if temperatures and pressures cross the water condensation curves shown in Fig. 9. Water condensation occurs below 400 K in the pressure range investigated here. In Fig. 9 the scales are expanded and extended P–T profiles for Jupiter, Gl 299B, and the M dwarf from Fig. 1 are also shown.

Water condensation temperatures increase as metallicity increases because the amount of oxygen (i.e., water) relative to hydrogen is higher with increasing metallicity. The condensation temperature of water as a function of total pressure (in bars) and metallicity is approximated by

$$10^4/T_{cond}(H_2O) = 38.84 - 3.93 \times [Fe/H] - 3.83 \times \log P_{tot} - 0.20 \times [Fe/H] \times \log P_{tot}. \quad (34)$$

Water condensation is only expected in the coolest atmospheres such as those of giant planets (Fig. 9). The P–T profile for Gl 229B from Marley *et al.* (1996) does not cross any water condensation temperature curves. Water vapor is expected to be a dominant opacity source in Gl 229B or other similar methane dwarfs and strong water bands are observed in Gl 229B and other T and L dwarfs (see references cited in the introduction).

Carbon dioxide, CO_2. Another important carbon and oxygen bearing gas is CO_2 and its abundances as a function of metallicity are shown in Figs. 10a–10c. Although it is not the major carbon-bearing gas in the P–T range here, carbon dioxide is fairly abundant when CO is the major carbon-bearing gas. A comparison of Figs. 5a–5c and 10a–10c shows that CO_2 is more abundant than CH_4 over a wide P–T range inside the CO dominance field. The CO_2 abundances throughout much of the CO field are independent of total pressure and depend only on temperature. Inside the CO dominance field CO_2 is formed via the net thermochemical reaction

$$CO + H_2O = CO_2 + H_2, \quad (35)$$

which has an equilibrium constant K_{35} given by

$$K_{35} = P_{CO_2}P_{H_2}/(P_{CO}P_{H_2O}) = X_{CO_2}X_{H_2}/(X_{CO}X_{H_2O}) \quad (36)$$

independent of total pressure. Rearranging to solve for the CO_2 mole fraction yields

$$X_{CO_2} = K_{35}[(X_{CO}X_{H_2O})/X_{H_2}]. \quad (37)$$

The quotient inside the square brackets is approximately constant because the CO and H_2O mole fractions can be replaced

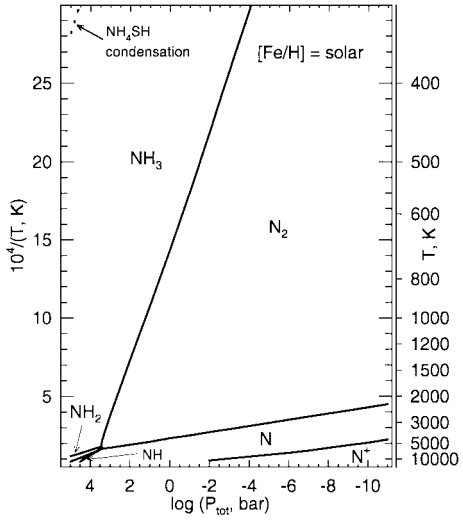

FIG. 17. The labeled regions map the presence of the major nitrogen-bearing gases as a function of P and T in a solar composition gas. The dividing lines show where the different gases have equal abundances (e.g., NH_3 and N_2). The dashed line indicates the condensation temperature of NH_4SH (s). The ammonia condensation temperatures are at lower temperatures than shown in the graph.

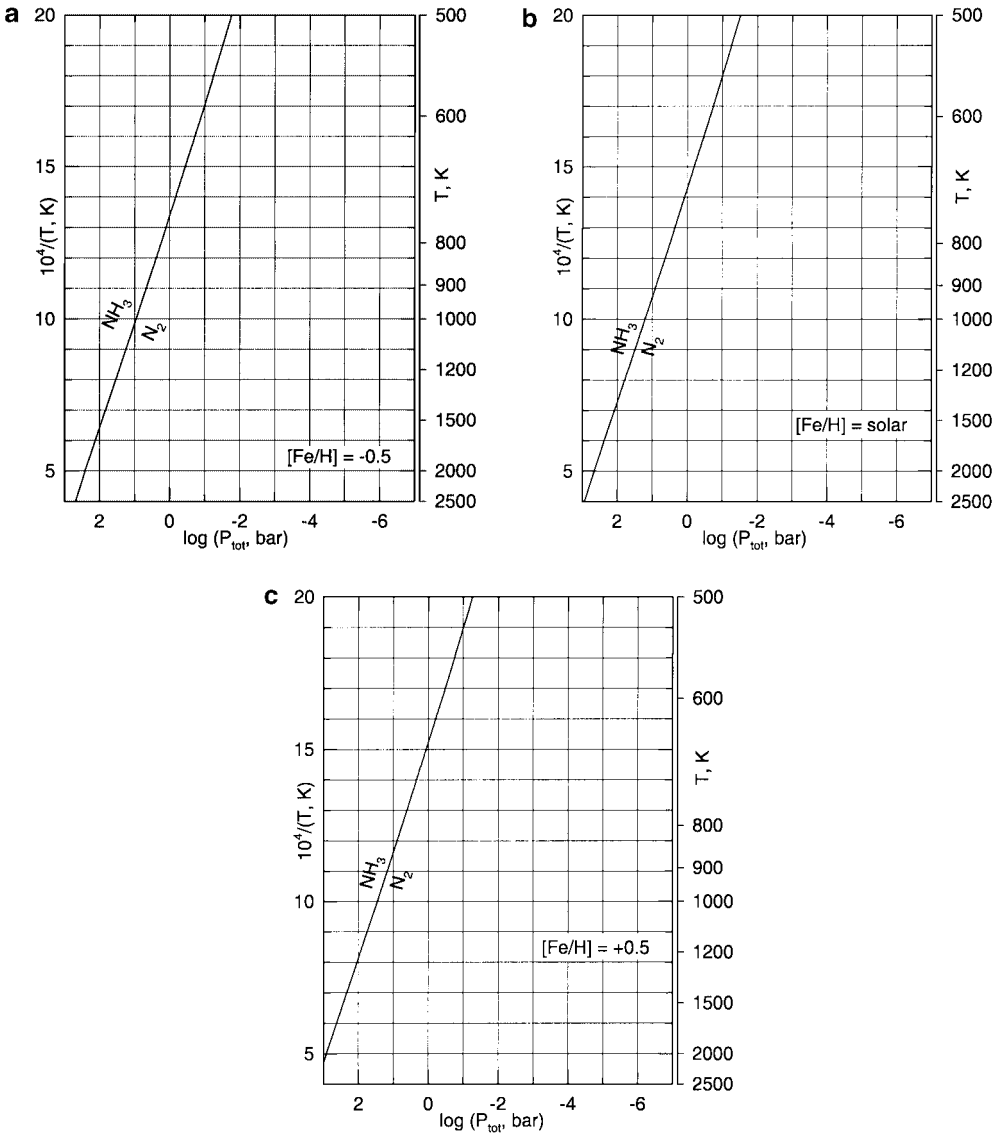

FIG. 18. The $NH_3 = N_2$ boundary, along which NH_3 and N_2 have equal abundances, as a function of pressure and temperature for subsolar (a), solar (b), and enhanced (c) metallicities.

by Eqs. (25) and (26) to give

$$X_{CO_2} = K_{35} X_{\Sigma C} \left(X_{\Sigma O_{gas}} - X_{\Sigma C} \right) / X_{H_2}. \quad (38)$$

Equation (38) is a function of temperature only until sufficiently high temperatures where H_2O thermal dissociation becomes appreciable.

The inflection points on the CO_2 mole fraction contours occur along the $CH_4 = CO$ boundary. The CO_2 mole fractions are a function of both temperature and pressure inside the field where CH_4 is the dominant C-bearing gas because there CO_2 is formed via the net thermochemical reaction

$$CH_4 + 2H_2O = CO_2 + 4H_2. \quad (39)$$

The equilibrium constant (K_{39}) for reaction (39) is

$$K_{39} = P_{CO_2} P_{H_2}^4 / \left(P_{CH_4} P_{H_2O}^2 \right) = X_{CO_2} X_{H_2}^4 / \left(X_{CH_4} X_{H_2O}^2 \right) P_T^2. \quad (40)$$

Rearranging to find the CO_2 mole fraction and substituting for X_{CH_4} and X_{H_2O} using the mass balance equations (31) and (32) gives

$$\begin{aligned} X_{CO_2} &= K_{39} X_{\Sigma C} (0.84 X_{\Sigma O})^2 / (0.833)^4 \cdot P_T^{-2} \\ &\cong 1.465\, K_{39} X_{\Sigma C} X_{\Sigma O_{gas}}^2 \cdot P_T^{-2}. \end{aligned} \quad (41)$$

Equation (41) shows that the CO_2 mole fraction is inversely proportional to $(P_T)^2$ and varies with temperature inside the CH_4

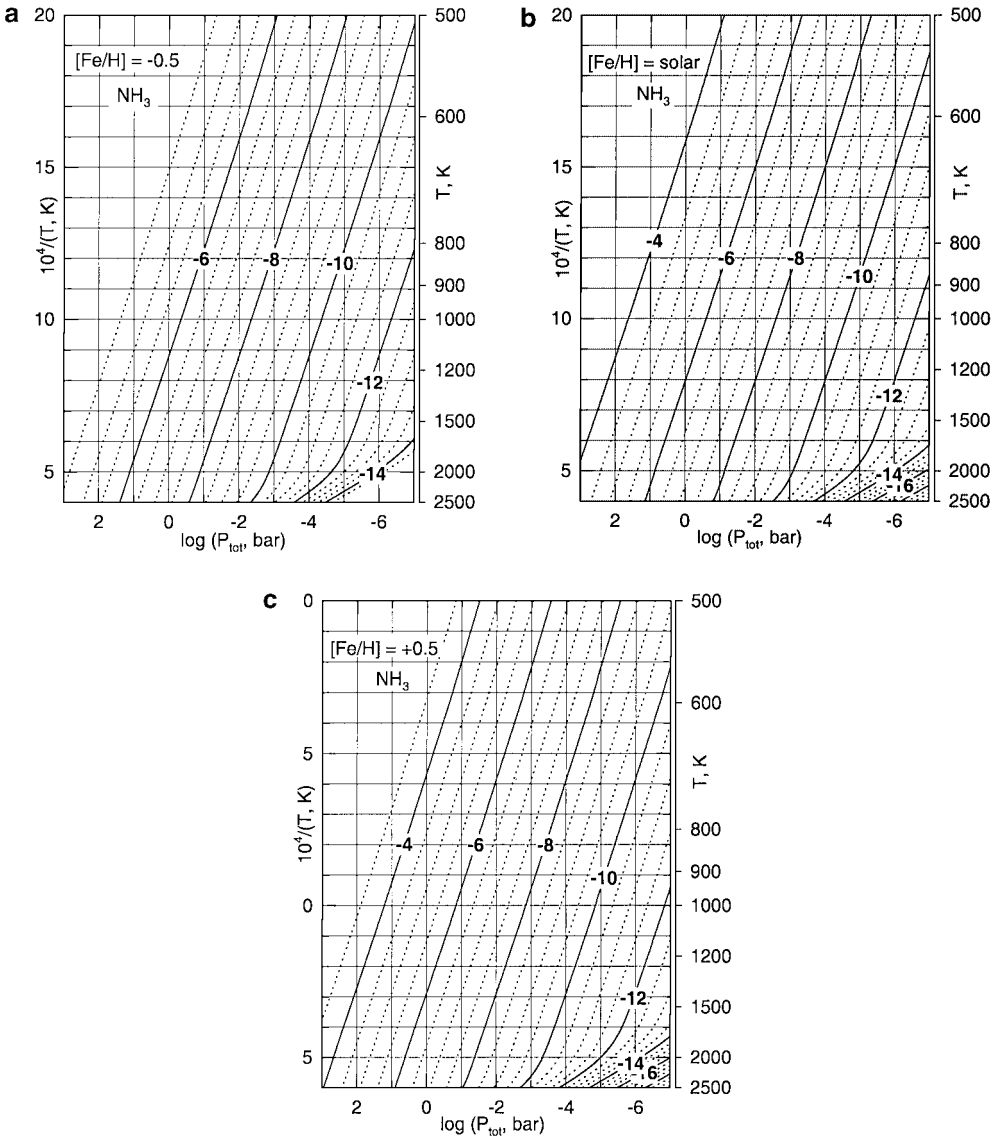

FIG. 19. Contours (on a logarithmic scale) of the ammonia (NH_3) mole fraction for subsolar (a), solar (b), and enhanced (c) metallicities.

field. The CO_2 mole fractions shown in Figs. 10a–10c are a potential temperature indicator for early L and M dwarfs, provided that the overall metallicity is known because higher metallicities favor higher CO_2 abundances for a given temperature and pressure.

Methyl, CH_3. The methyl radical is among the next most abundant hydrocarbons after methane. Methyl mole fractions are shown in Figs. 11a–11c as a function of metallicity. Inside the CH_4 field, CH_3 radicals are formed by thermal dissociation of CH_4

$$CH_4 = CH_3 + H, \tag{42}$$

and their abundance is inversely proportional to total pressure

$$X_{CH_3} = K_{42} X_{CH_4} / X_H \cdot P_T^{-1}. \tag{43}$$

Inside the CO field, CH_3 radicals form via the net reaction

$$CO + 3H_2 = H_2O + CH_3 + H \tag{44}$$

and their abundance is proportional to total pressure

$$\begin{aligned} X_{CH_3} &= K_{44} X_{CO} X_{H_2}^3 / \left(X_{H_2O} X_H\right) \cdot P_T \\ &\cong 0.578 \cdot K_{44} X_{\Sigma C} / \left(X_{\Sigma O_{gas}} - X_{\Sigma C}\right) \cdot P_T / X_H. \end{aligned} \tag{45}$$

The CH_3 abundance contours are relatively insensitive to temperature and are nearly parallel to isobars inside the CO field, and are potential pressure indicators for early L and M dwarfs of known metallicity. Methyl radicals formed by solar UV driven photochemistry have been observed in the upper atmospheres of Saturn and Neptune (Bezard *et al.* 1998, 1999) at column

densities of (2.5–6.0) × 10^{13} on Saturn and (0.7–2.8) × 10^{13} on Neptune. The corresponding mixing ratios are a few 100 ppb. Similar CH_3 mole fractions are expected in the deep atmospheres of T dwarfs such as Gl 299B.

Ethane, C_2H_6. Ethane is the second most abundant hydrocarbon after methane. Mole fraction contours of ethane are shown in Figs. 12a–12c for different metallicities. Ethane abundances decrease with decreasing temperatures and pressures in the CO field. In contrast, C_2H_6 abundances are pressure independent over wide ranges in the CH_4 dominance field. This behavior occurs because the equilibrium constant for C_2H_6 formation from methane is not a function of pressure:

$$2CH_4 = C_2H_6 + H_2 \tag{46}$$

$$K_{46} = P_{C_2H_6}P_{H_2}/P^2_{CH_4} = X_{C_2H_6}X_{H_2}/X^2_{CH_4}. \tag{47}$$

The ethane abundances inside the CH_4 field are diagnostic of temperature if the metallicity is known and if all C_2H_6 is thermochemical in origin. The latter condition is definitively not true for the gas giant planets in our solar system where the observed C_2H_6 is produced photochemically. The relative importance of photochemical and thermochemical sources for C_2H_6 in Gl 229B and in other T dwarfs, especially those that are "free floating," has not yet been evaluated. Finally, we note that propane (C_3H_8, not shown) displays behavior similar to ethane, but has abundances about 10 orders of magnitude lower.

Ethylene, C_2H_4 and acetylene, C_2H_2. The abundances of these two hydrocarbons are plotted in Figs. 13a–13c and 14a–14c. The inflection points in the contours occur at the CH_4 = CO boundary (Fig. 4) and arise because of the different net thermochemical reactions that are responsible for formation of C_2H_4 and C_2H_2 in the CH_4 and CO dominance fields. Inside the CH_4 field, C_2H_4 forms via the net reaction

$$2CH_4 = C_2H_4 + 2H_2, \tag{48}$$

and the C_2H_4 mole fraction is given by

$$X_{C_2H_4} = K_{48}X^2_{CH_4}/X^2_{H_2} \times P_T^{-1} \cong 1.44\, K_{48}X^2_{\Sigma C} \times P_T^{-1}, \tag{49}$$

where X_{H_2} is taken as constant at these near-solar metallicities. In the CO field, ethylene is formed via the net reaction

$$2CO + 4H_2 = C_2H_4 + 2H_2O, \tag{50}$$

which leads to

$$X_{C_2H_4} = K_{50}\, X^2_{CO}X^4_{H_2}/X^2_{H_2O} \times P_T^3 \cong 0.481\, K_{50}X^2_{\Sigma C}/\left(X_{\Sigma O_{gas}} - X_{\Sigma C}\right)^2 \times P_T^3. \tag{51}$$

The C_2H_4 abundance is inversely proportional to the total pressure inside the CH_4 field and proportional to $(P_T)^3$ inside the CO field. Similarly, C_2H_2 is formed via the net reaction

$$2CH_4 = C_2H_2 + 3H_2 \tag{52}$$

inside the CH_4 field and via the net reaction

$$2CO + 3H_2 = C_2H_2 + 2H_2O \tag{53}$$

inside the CO field. The corresponding expressions for the variation of the C_2H_2 abundance with pressure are

$$X_{C_2H_2} = K_{52}X^2_{CH_4}/X^3_{H_2} \times P_T^{-2} \cong 1.73K_{52}X^2_{\Sigma C} \times P_T^{-2} \tag{54}$$

inside the CH_4 field and

$$X_{C_2H_2} = K_{53}X^2_{CO}X^3_{H_2}/X^2_{H_2O} \times P_T^2 \cong 0.578\, K_{53}X^2_{\Sigma C}/\left(X_{\Sigma O_{gas}} - X_{\Sigma C}\right)^2 \times P_T^2 \tag{55}$$

inside the CO field. As a consequence, the C_2H_2 abundance is inversely proportional to $(P_T)^2$ inside the methane field but directly proportional to $(P_T)^2$ inside the CO field.

Figures 12 and 13 indicate that C_2H_4 mole fractions of about 0.1 ppb to a few ppb are expected in the deep atmospheres of T dwarfs. These abundances are comparable to those of C_2H_4 in Jupiter's atmosphere. Acetylene mole fractions of 0.1 ppb to ~10 ppb are expected in the deep atmospheres of T dwarfs such as Gl 229B. This is about 100 times smaller than C_2H_2 mole fractions in the jovian atmosphere. Smaller amounts of C_2H_4 and C_2H_2 are expected in the atmospheres of L and M dwarfs.

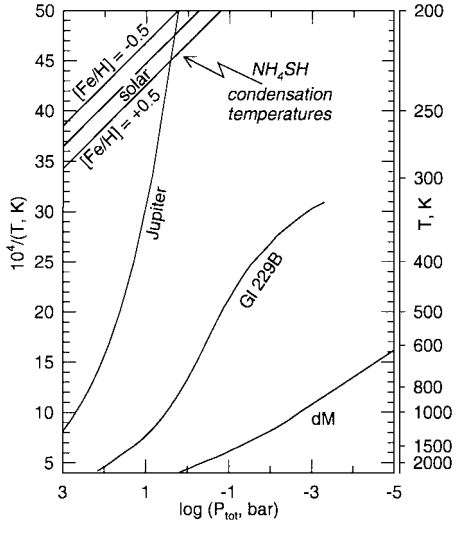

FIG. 20. A plot of solid ammonium hydrosulfide (NH_4SH) condensation curves for subsolar, solar, and enhanced metallicity systems. Solid NH_4SH is stable on and above the condensation curves. These curves intersect the P, T profile for Jupiter, where solid NH_4SH clouds are expected, but do not intersect the P, T profiles for Gliese 229B or the M dwarf, where solid NH_4SH clouds are not expected.

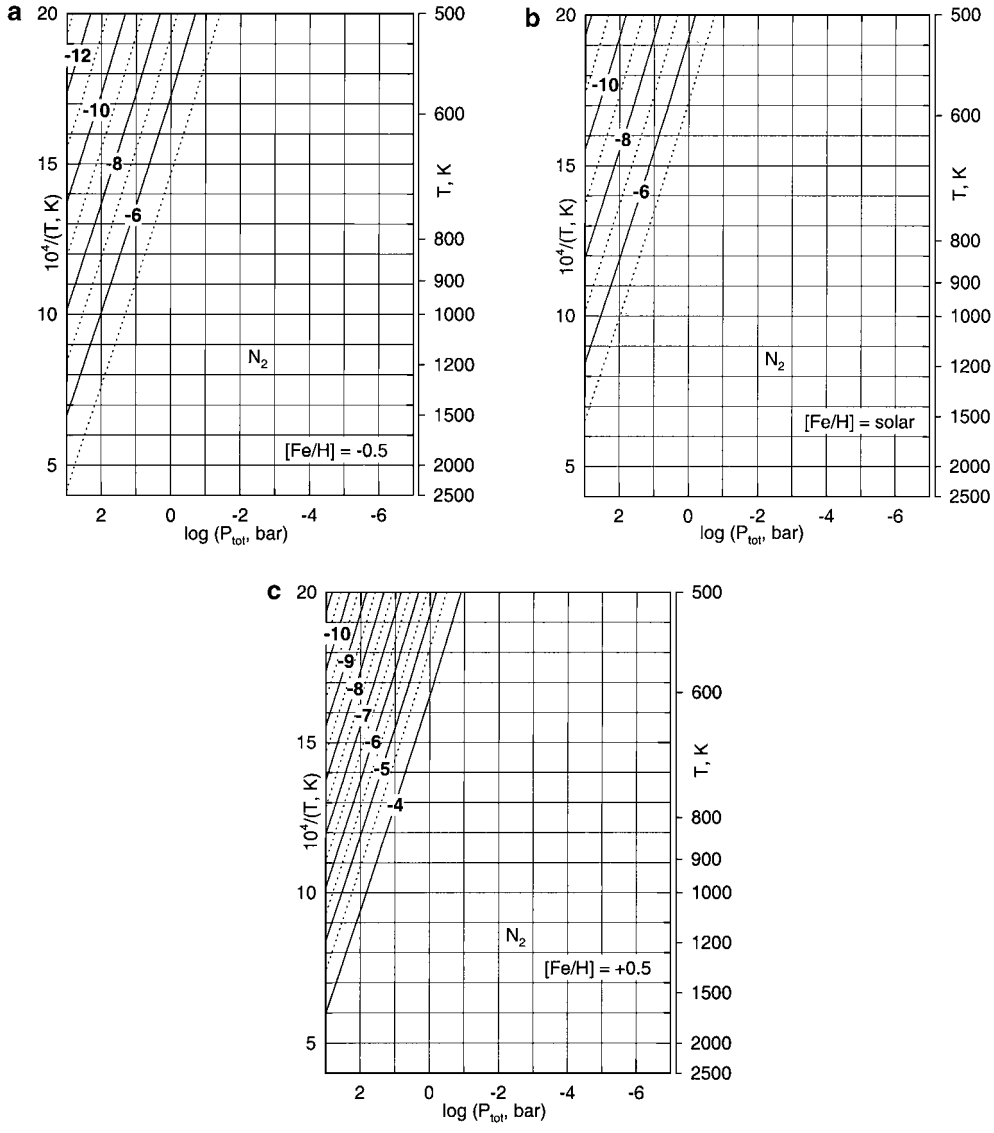

FIG. 21. Contours (on a logarithmic scale) of the molecular nitrogen (N_2) mole fraction for subsolar (a), solar (b), and enhanced (c) metallicities.

Finally, the photochemical contribution to C_2H_4 and C_2H_2 in the deep troposphere of T dwarfs remains to be assessed.

Formaldehyde, CH_2O. Formaldehyde is among the more abundant oxygen-bearing organics. Figures 15a–15c display the CH_2O abundance contours as a function of metallicity. The points of inflection where formaldehyde mole fractions peak in P–T space, follow again the $CH_4 = CO$ boundary (Fig. 4). Inside the methane field, formaldehyde forms via the net reaction

$$CH_4 + H_2O = CH_2O + 2H_2, \tag{56}$$

and its abundance is inversely proportional to total pressure

$$X_{CH_2O} = K_{56} X_{CH_4} X_{H_2O} / X_{H_2}^2 \times P_T^{-1} \cong 1.441\, K_{56} X_{\Sigma C} X_{\Sigma O_{gas}} \times P_T^{-1}. \tag{57}$$

Inside the CO field, CH_2O forms via

$$CO + H_2 = CH_2O, \tag{58}$$

and its abundance increases linearly with total pressure

$$X_{CH_2O} = K_{58} X_{CO} X_{H_2} \times P_T \cong 0.833 K_{58} X_{\Sigma C} \times P_T. \tag{59}$$

The CH_2O mole fraction contours are relatively insensitive to total pressure inside the CO field because K_{58} only varies weakly with temperature. Thus, CH_2O is potentially a pressure indicator in L and M dwarfs. The expected formaldehyde abundances in the deep atmospheres of T dwarfs are ∼0.1–10 ppb depending on P, T, and metallicity.

Methanol, CH_3OH. Methanol abundance contours are plotted in Figs. 16a–16c. The contours are independent of total pressure inside the methane field where CH_3OH forms via the net reaction

$$CH_4 + H_2O = CH_3OH + H_2. \quad (60)$$

Rearranging the equilibrium constant expression for this reaction gives

$$X_{CH_3OH} = K_{60} X_{CH_4} X_{H_2O} / X_{H_2} \cong 1.20 K_{60} X_{\Sigma C} X_{\Sigma O_{gas}}, \quad (61)$$

which shows that the CH_3OH abundance is a function only of temperature. In contrast, inside the CO dominance field, CH_3OH is formed via the net reaction

$$CO + 2H_2 = CH_3OH, \quad (62)$$

which leads to a dependence upon $(P_T)^2$ for the CH_3OH mole fraction

$$X_{CH_3OH} = K_{62} X_{CO} X_{H_2}^2 \cdot P_T^2 \cong 0.694\, K_{62} X_{\Sigma C} \cdot P_T^2. \quad (63)$$

Methanol abundances in the deep atmospheres of T dwarfs are predicted to be about 0.01–0.1 ppb, and in principle, can be used as a temperature indicator. Methanol abundances of 0.1 ppb are expected at the kilobar level in Jupiter's atmosphere.

Other carbon- and oxygen-bearing gases. Many other carbon- and oxygen-bearing gases are present at equilibrium under the conditions investigated here. Table I gives a list of species in order of decreasing abundance for three different pressures at 1000 K to illustrate what species are the most important ones. Except for those compounds noted in the text, no other compounds can be used to serve as either pressure or temperature indicators.

Nitrogen Chemistry

The major features of nitrogen chemistry are similar to those of carbon. Figure 17, which is analogous to Figs. 2 and 3, shows the major nitrogen-bearing gases over a wide range of pressure and temperatures; the lines show where the different nitrogen-bearing gases have equal abundances. The distribution of nitrogen between the major gases NH_3 and N_2 is described by the equilibrium

$$0.5N_2 + 1.5H_2 = NH_3, \quad (64)$$

which depends on temperature and total pressure. At high pressures, ammonia gas dominates, and at low pressures, N_2 gas dominates, but the NH_3 to N_2 transition is favored by higher temperatures. At the highest temperatures shown, thermal dissociation of N_2 to atomic N and subsequent thermal ionization to N^+ take place at low pressures while at high pressures NH_3 dissociates to NH_2 and NH. On the other hand, at the lowest temperatures (and highest pressures) shown, NH_4SH condensation takes place, followed by solid ammonia condensation at even lower temperatures (see discussion below).

Figures 18a–18c show the $NH_3 = N_2$ boundary, where ammonia gas and N_2 have the equal abundances as a function of metallicity. Although NH_3 and N_2 have equal abundances along this line, the fraction of total nitrogen in each of the two gases is different with $\sim 1/3$ in NH_3 and $2/3$ in N_2. A comparison of Fig. 18 with the P–T profiles from Fig. 1 shows that the major N-bearing gas in cool T dwarfs and giant planets is NH_3, while N_2 is the major N-bearing gas in L and M dwarfs.

The $NH_3 = N_2$ boundaries in Fig. 18 are located at considerably lower temperatures and higher pressures than the corresponding $CH_4 = CO$ boundaries (Fig. 4) for a given metallicity. Higher metallicities shift the $NH_3 = N_2$ boundary to lower temperatures and higher pressures. Any object showing NH_3 is expected to show methane as the major carbon-bearing gas. The gas giant planets in our solar system have essentially all of their nitrogen as NH_3 in their observable atmospheres because their atmospheric P–T structures fall into the ammonia field (for NH_3 condensation see below). Brown dwarfs such as Gl 229B are borderline objects because the P–T profile of Gl 299B just cuts through the $NH_3 = N_2$ boundaries at low temperatures. Ammonia has been tentatively detected in Gl 299B by Saumon *et al.* (2000). A comparison of Fig. 1 with the $NH_3 = N_2$ boundaries in Fig. 18 shows that the P–T profile for Gl 229B crosses the $NH_3 = N_2$ boundary at lower temperatures for higher metallicities. In low-mass M dwarfs with atmospheric P–T characteristics as shown in Fig. 1, N_2 is always the major N-bearing gas.

Ammonia, NH_3. As discussed above for CO and methane, NH_3 is still present in some amounts when N_2 is the major

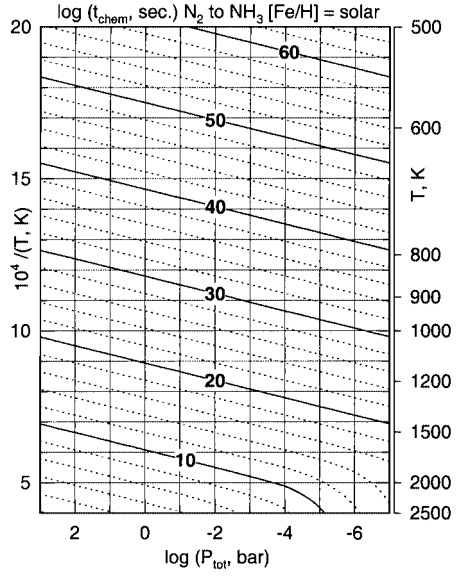

FIG. 22. Logarithmic time scale (seconds) contours for the chemical conversion of N_2 to NH_3. The conversion of N_2 to NH_3 is favored at high pressures and high temperatures.

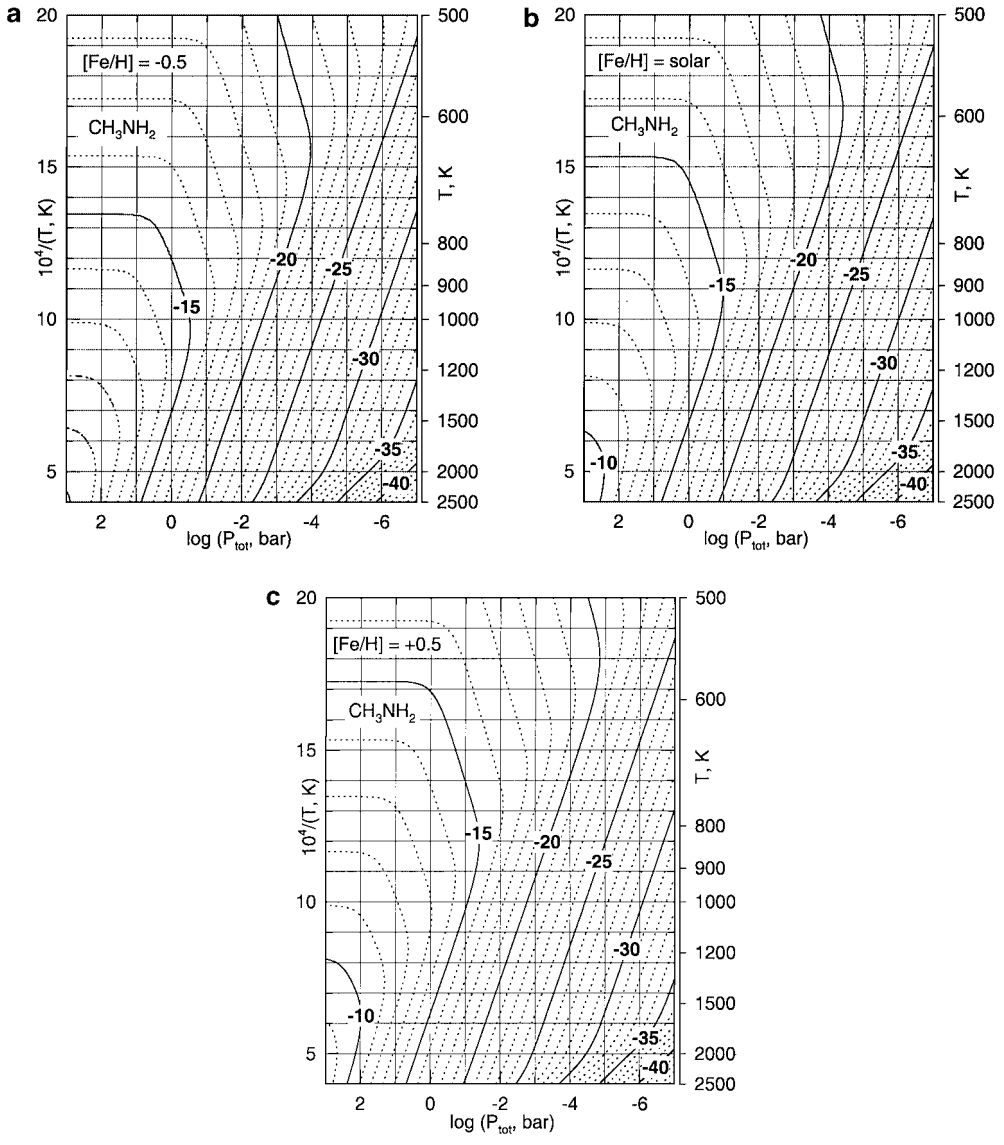

FIG. 23. Contours (on a logarithmic scale) of the methylamine (CH_3NH_2) mole fraction for subsolar (a), solar (b), and enhanced (c) metallicities.

N-bearing gas. The mole fractions of NH_3 are shown in Figs. 19a–19c as a function of metallicity, P and T. Abundances decrease as temperatures and total pressure decrease when moving away from the $NH_3 = N_2$ boundaries. At given temperature and pressure, ammonia abundances are larger at higher metallicities relative to solar, because of the relatively higher N/H ratio. Figures 19a–19c indicate that ammonia may be present in detectable amounts even when N_2 is the more abundant gas and the use of the $NH_3 = N_2$ boundary as a temperature indicator has the same problems and uncertainties as discussed above for the estimation of the temperature from the CO-CH_4 boundary.

We can devise a similar formalism for the ammonia dependence on metallicity as done above for the metallicity dependence of the methane and CO abundances. The mole fractions of ammonia in the field where N_2 is the major gas are described by using the equilibrium constant of Eq. (64)

$$X_{NH_3} = K_{64} X_{N_2}^{0.5} X_{H_2}^{1.5} \times P_T. \tag{65}$$

Using the approximation that essentially all nitrogen is found as N_2, which is true a relatively short distance from the $NH_3 = N_2$ boundary inside the N_2 field, we can substitute $X(N_2) = 0.5X_{\Sigma N}$. Introducing again the metallicity factor "m," Eq. (65) becomes

$$X_{NH_3} = K_{64}(m \times 0.5X_{\Sigma N})^{0.5} X_{H_2}^{1.5} \times P_T, \tag{66}$$

which shows that the mole fractions of ammonia in the N_2 field are proportional to total pressure and proportional to $m^{0.5}$.

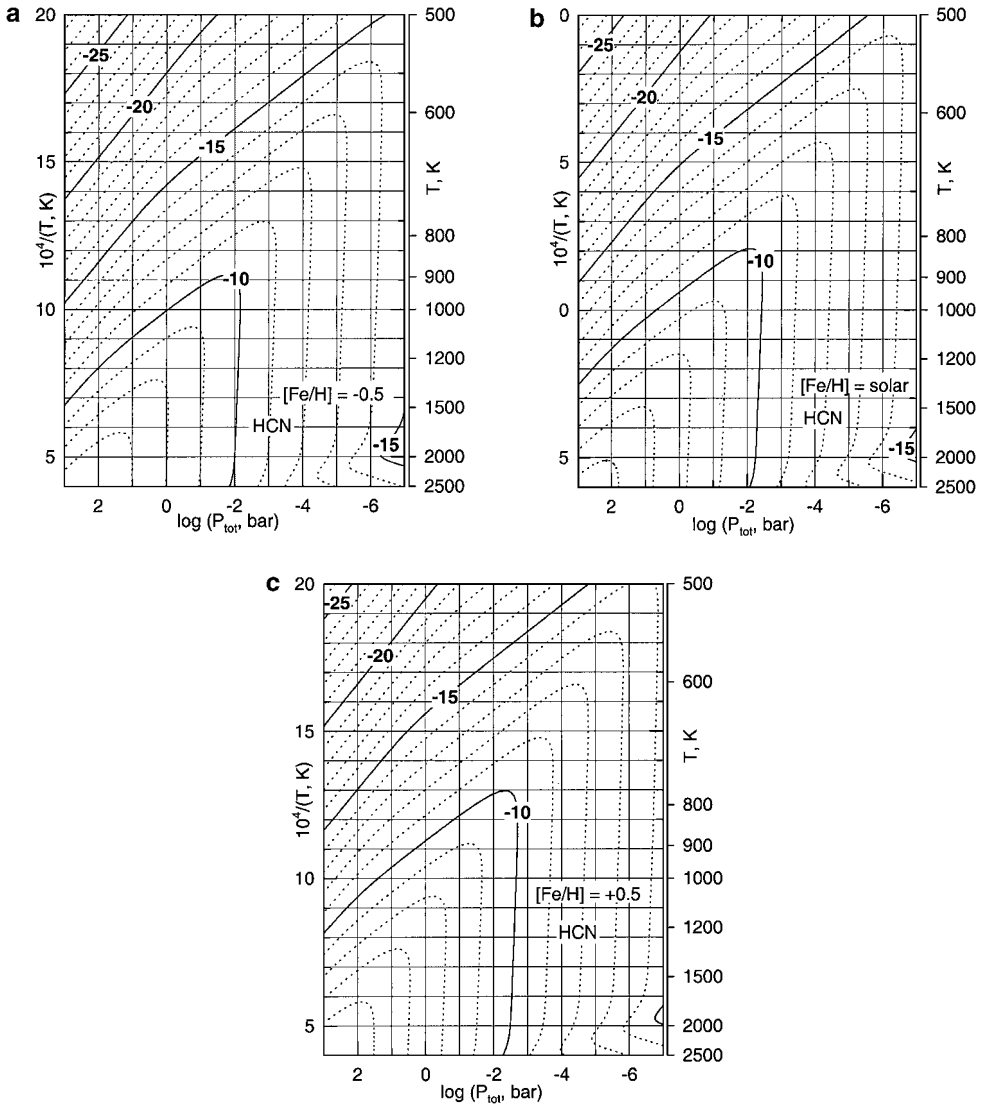

FIG. 24. Contours (on a logarithmic scale) of the hydrogen cyanide (HCN) mole fraction for subsolar (a), solar (b), and enhanced (c) metallicities.

Condensation of ammonium hydrogen sulfide and ammonia NH_4SH (s), NH_3 (s). In the coolest atmospheres, NH_4SH (s) and NH_3 (s) condensation may take place and cause ammonia vapor removal from the upper parts of the atmosphere. Solid ammonia clouds are observed and NH_4SH (s) clouds are strongly suspected for the giant planets Jupiter and Saturn. Ammonium hydrosulfide is the first major ammonium bearing condensate and its condensation temperatures are shown for three metallicities in Fig. 20 (note the extended temperature axis). Higher metallicities (i.e., higher N/H and S/H ratios than solar) cause an increase in condensation temperatures. The NH_4SH (s) condensation temperatures as a function of total pressure and metallicity are approximated by

$$10^4/T_{cond}(NH_4SH,\ s) = 48.94 - 4.27[Fe/H] - 4.15 \times \log P_{tot}. \quad (67)$$

The amount of nitrogen removed from the atmosphere by NH_4SH condensation is limited by the abundance of H_2S gas. Essentially, all sulfur is tied up in H_2S gas (only about 2.5% of all sulfur is removed into Na_2S solid and liquid at higher T; see Lodders 1999a). The atomic abundance ratio of sulfur to nitrogen is ~0.17 (independent of the metallicities considered here) so ample NH_3 remains in the gas after NH_4SH condensation. The remaining ammonia gas condenses as ammonia solid or liquid, but only at lower temperatures than NH_4SH condenses. The condensation temperatures of ammonia as a function of total pressure and metallicity are approximated by

$$10^4/T_{cond}(NH_3) = 68.02 - 6.19 \times [Fe/H] - 6.31 \times \log P_{tot}. \quad (68)$$

Figure 20 includes the P–T profiles for the three types of low-mass objects. Ammonia gas becomes depleted only in the

upper atmospheres of objects whose P–T profiles cross the NH_4SH condensation curves, which is found for Jupiter. In T dwarfs such as Gl 229B, removal of ammonia by condensation is not expected and is of no relevance in warmer L and M dwarfs, where ammonia gas never is the major nitrogen-bearing gas to begin with.

Diatomic nitrogen, N_2. Mole fractions of diatomic nitrogen decrease from the $NH_3 = N_2$ boundary toward lower temperatures and higher pressures in the ammonia field, as shown for different metallicities in Figs. 21a–21c. The N_2 mole fractions are sensitive to metallicity; for example, at subsolar metallicities, N_2 abundances are smaller than at solar metallicity at a given T and P. The N_2 abundances in the ammonia field are derived similarly to those discussed above for CH_4, CO or NH_3 and we obtain for the mole fraction of N_2

$$X_{N_2} = K_{64}^{-2}(m \cdot X_{\Sigma N})^2 / X_{H_2}^3 \times P_T^{-2} \quad (69)$$

The mole fractions of N_2 are inversely proportional to total pressure squared and proportional to the square of the metallicity factor m.

N_2 Chemical Reaction Time Scales

Figure 22 gives the chemical time scales for the N_2 to NH_3 conversion ($\log t_{chem}$ in seconds) as a function of temperature and pressure. The details for the calculation of these reaction time scales are given in Fegley and Lodders (1994). The rate determining step for homogeneous gas phase conversion of N_2 to NH_3 is the reaction of molecular H_2 plus N_2 to NH (imidogen) and the chemical lifetime of N_2 depends on the molecular number densities of H_2 (denoted by square brackets):

$$t_{chem}(N_2) = 1/\{k_{N_2}[H_2]\}. \quad (70)$$

The kinetic rate constant $k_{N_2} = 8.45 \times 10^{-8} \exp(-81{,}515/T)$, in cm^3/s, is from Lewis and Prinn (1980). The conversion is fastest at high pressures and temperatures, but very slow at low temperatures and low pressures. Comparison of these time scales with the nominal P–T profiles in Fig. 1 shows that the N_2 to NH_3 conversion is quenched very deep in the atmospheres of gas giant planets and T dwarfs. Interestingly, these deep levels are inside the ammonia field for gas giant planets such as Jupiter, but are inside the N_2 field for T dwarfs such as Gl 229B. The thermodynamics and kinetics of the N_2 to NH_3 conversion predict that NH_3 is the major N-bearing gas and N_2 is a minor N-bearing gas in the gas giant planets, but predict the opposite for T dwarfs. These results, first presented by Lodders (1999c) are consistent with the tentative detection of NH_3 in Gl 229B (Saumon *et al.* 2000). Likewise, NH_3 is predicted to be a minor species while N_2 is the major N-bearing gas in the atmospheres of L and M dwarfs on both thermodynamic and kinetic grounds.

Methylamine, CH_3NH_2. Among the abundant N-bearing gases at higher pressures and lower temperatures is CH_3NH_2. The abundance contours in Figs. 23a–23c have inflections at the location of the CO = methane boundaries (Fig. 4) and of the $NH_3 = N_2$ boundaries (Fig. 18), showing the profound influence of the major gas boundaries on trace gas chemistry. Trace amounts of methylamine (0.1 ppb) may be present in the deep atmospheres of gas giant planets and T dwarfs. A comparison of the mole fractions of CH_3NH_2 in Figs. 23a–23c and the P–T profiles in Fig. 1 indicates that CH_3NH_2 abundances in L and M dwarfs are insignificant.

Hydrogen cyanide, HCN. Among the more abundant N-bearing gases after N_2 and NH_3 is HCN, for which the mole fractions are shown in Figs. 24a–24c as function of metallicity. An increase in metallicity increases the HCN mole fractions at a given temperature and pressure. The mole fraction contours show much more curvature than those for N_2 or NH_3. The highest abundances of HCN are found at high pressures and high temperatures in the ammonia stability field. With decreasing temperatures (at high total pressures) HCN abundances drop and the equilibrium abundances are low in giant planets and cool brown dwarf atmospheres. In objects where N_2 is the major gas, HCN abundances are sensitive to total pressure but not very sensitive to temperatures and HCN abundances can be used as a pressure probe in early L and M dwarfs.

There are three qualitatively different regions of major abundant gases determining the HCN chemistry (1) CH_4 and NH_3, (2) CH_4 and N_2, and (3) CO and N_2. In the CH_4 and NH_3 region, HCN is formed via the net reaction

$$CH_4 + NH_3 = HCN + 3H_2. \quad (71)$$

Using the equilibrium constant expression for Eq. (71), the HCN

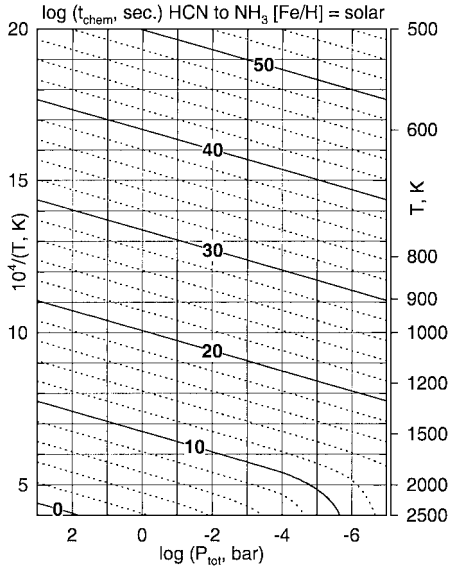

FIG. 25. Logarithmic time scale (seconds) contours for the chemical conversion of HCN to NH_3. The conversion of HCN to NH_3 is favored at high pressures and high temperatures.

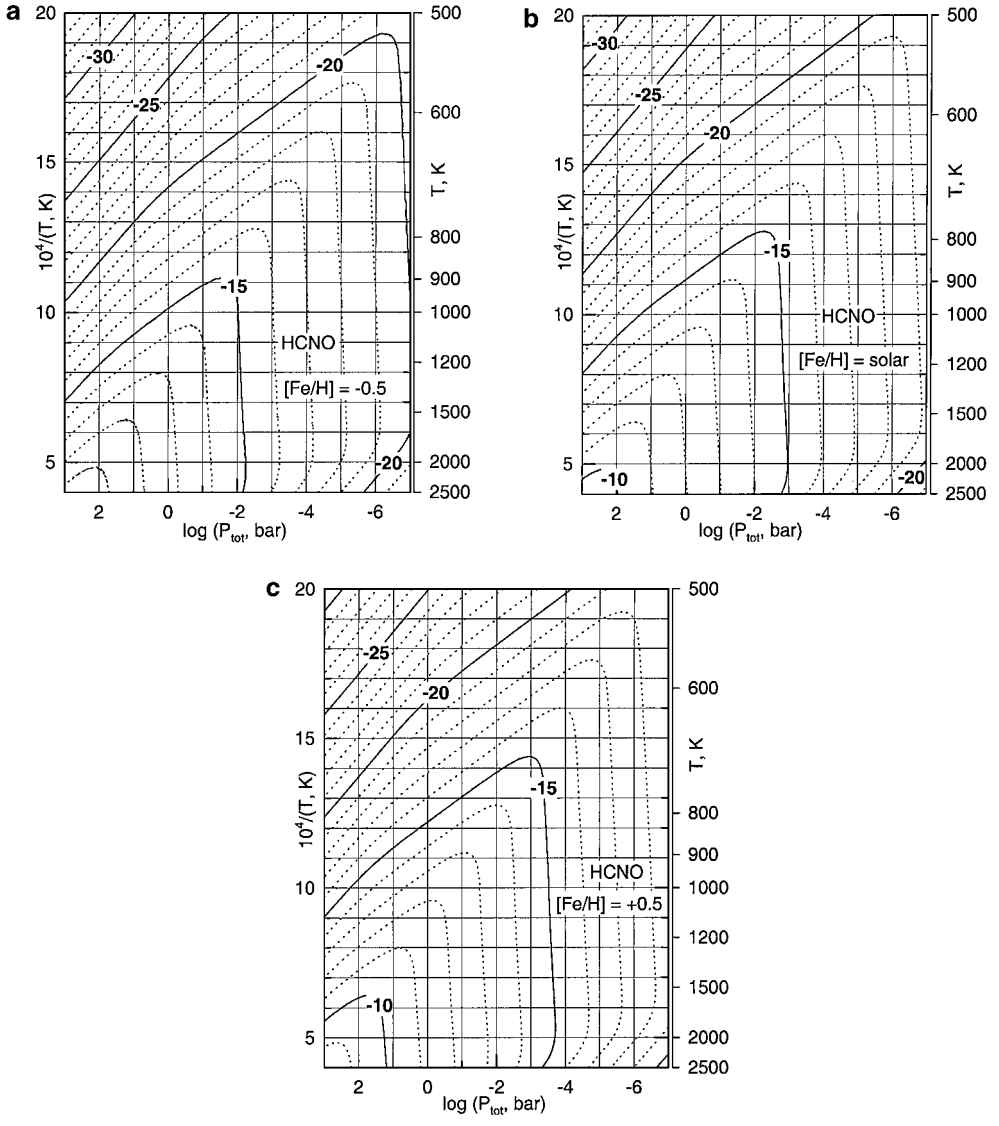

FIG. 26. Contours (on a logarithmic scale) of the hydrogen isocyanate (HCNO) mole fraction for subsolar (a), solar (b), and enhanced (c) metallicities.

mole fraction is given by

$$X_{HCN} = K_{71}(X_{CH_4}X_{NH_3})/X_{H_2}^3 \times P_T^{-2} \cong 1.728\, K_{71}X_{\Sigma N}X_{\Sigma C} \times P_T^{-2} \quad (72)$$

and is inversely proportional to the square of total pressure. In the CH_4 and N_2 region, HCN forms via the net reaction

$$CH_4 + 0.5N_2 = HCN + 1.5H_2. \quad (73)$$

The HCN mole fraction is then given by

$$X_{HCN} = K_{74}X_{CH_4}X_{N_2}^{0.5}/X_{H_2}^{1.5} \times P_T^{-1} \cong 1.315\, K_{74}X_{\Sigma C}(0.5X_{\Sigma N})^{0.5} \times P_T^{-1} \quad (74)$$

and is inversely proportional to the total pressure. Finally, in the region of major CO and N_2, HCN forms via the net reaction

$$CO + 1.5H_2 + 0.5N_2 = HCN + H_2O. \quad (75)$$

The HCN mole fraction is obtained from

$$X_{HCN} = K_{75}X_{CO}X_{N_2}^{0.5}X_{H_2}^{1.5}/X_{H_2O} \times P_T \cong 0.761K_{75}X_{\Sigma C}(0.5X_{\Sigma N})^{0.5}/X_{\Sigma O_{gas}} \times P_T \quad (76)$$

and is proportional to the total pressure.

HCN Chemical Reaction Time Scales

Figure 25 shows the chemical time scales for the HCN to NH_3 conversion ($\log t_{chem}$ in seconds) as a function of temperature and

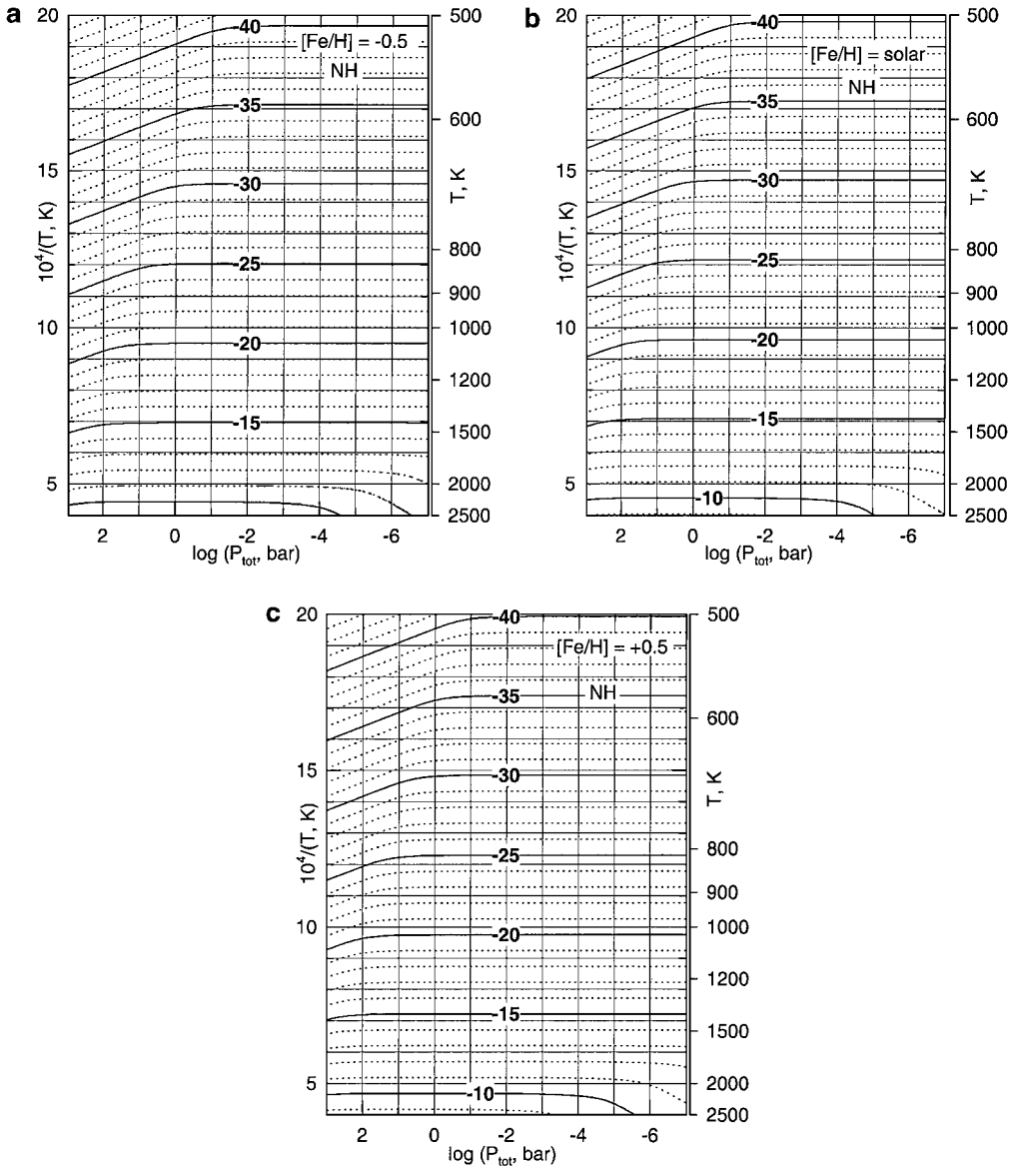

FIG. 27. Contours (on a logarithmic scale) of the imidogen (NH) mole fraction for subsolar (a), solar (b), and enhanced (c) metallicities.

pressure. The conversion is fastest at high pressures and temperatures, but very slow at low temperatures and low pressures. The kinetic modeling is described in Fegley and Lodders (1994). The rate determining step of converting HCN to NH_3 is the reaction of HCN plus molecular H_2 to CH_2 and NH, and the chemical lifetime of HCN depends on the molecular number densities of H_2 (denoted by square brackets),

$$t_{chem}(HCN) = 1/\{k_{HCN}[H_2]\} \quad (77)$$

and the kinetic rate constant $k_{HCN} = 1.08 \times 10^{-8}\ \exp(-70{,}456/T)$, in cm^3/s, from Lewis and Prinn (1980). If quenching occurs at t_{chem} values of 10^6–10^8 seconds then HCN mole fractions of 0.1–1 ppm are implied by Figs. 1 and 24 for T dwarfs such as Gl 229B. If slower convective mixing leading to quenching at larger t_{chem} values of 10^8–10^{10} seconds is assumed, then HCN mole fractions of $\leq$0.1 ppm are implied for Gl 229B-like T dwarfs. Because of the shape of the HCN mole fraction contours, HCN abundances of 1–10 ppb are implied for M dwarfs, and intermediate abundances of 10 ppb to 0.1 ppm for L dwarfs, for quenching at similar t_{chem} values.

Hydrogen isocyanate, HCNO. The abundances of HCNO are shown in Figs. 26a–26c. Its chemistry is similar to that of HCN but HCNO abundances are about five orders of magnitude lower than those of HCN at a given P and T. The HCNO figures are included because HCNO abundances are potential pressure probes for early L and M dwarf atmospheres.

Imidogen, NH. Among the minor abundant N-bearing gases, NH is a good temperature indicator because its mole fractions are virtually independent of total pressure for the pressure range covered here (Figs. 27a–27c). The NH mole fractions are below 10^{-20} at T < 1000 K for all metallicities and detection of this temperature probe is probably only possible in the deep atmospheres of L dwarfs and photospheres of M dwarfs. This is the only compound among the C-, N-, and O-bearing compounds investigated here which shows a pressure-independent distribution over a wide total pressure range.

Other N-bearing compounds. Table I lists other N-bearing compounds that are next most abundant after N_2, NH_3, CH_3NH_2, and HCN. There are no other major abundant N-bearing gases which could be used as either temperature or pressure indicators.

IMPLICATIONS AND CONCLUSIONS

The equilibrium thermochemistry for carbon, oxygen, and nitrogen reveals the following trends in chemical speciation: Methane and ammonia formation are favorable at low temperatures, high total pressures, and low metallicities. The presence or absence of major CO, N_2, CH_4, and/or NH_3 establishes a relative effective temperature scale and indicates that five potential types of objects exist: (1) Objects with major CO and N_2 have the highest effective temperatures; these are most likely low-mass early L and M dwarfs. (2) Next are objects with major CH_4 and N_2; these are in the methane brown dwarf (T dwarfs) category. (3) The objects with the coolest effective temperatures show major CH_4 and NH_3, which are very cool brown dwarf candidates (late T dwarfs). The brown dwarf Gl 229B is a borderline case for this cool T-dwarf scale. G1570D, one of the coolest T dwarfs with T_{eff} in the range of 784–824 K (Burgasser *et al*. 2000a, Geballe *et al*. 2001) may fall into the methane plus ammonia group. All objects with CH_4 and ammonia bands are expected to have water vapor if their atmospheres are sufficiently hot to prevent water condensation. Again, Gl 229B whose model P–T just "misses" the water condensation curve is a borderline case. (4) The fourth type of object is cool enough so that water condenses into clouds and they show methane and ammonia bands. (5) Among the fifth type of objects are very cool, giant planet-like objects, which only show methane but no ammonia, because ammonia has condensed as NH_4SH and/or NH_3. Such cool objects lack water vapor in their upper atmospheres, because water condenses at higher temperatures (greater depth) in the atmosphere than does ammonia.

The presence of CH_4 alone does not constrain temperature, and an abundance determination of methane is needed to obtain a reasonable temperature estimate. The abundance of methane is temperature and pressure dependent. If total pressure (or temperature) is independently determined and abundances of CH_4 are known, the temperature (or pressure) is uniquely defined.

The mole fractions of methane are relatively metallicity independent under conditions where CO is the major C-bearing gas and the abundance of CH_4 provides a metallicity independent constraint on the temperature. At constant T and P, mole fractions of other species discussed here generally show an increase when metallicity is increased.

Several other temperature and pressure indicators are identified. These species may prove useful if there are spectral windows that allow their detection deep in the atmosphere. For giant planets and cool methane dwarfs, the deep atmospheric abundances of ethane (Fig. 12) and methanol (Fig. 16) are diagnostic temperature probes because their abundances are relatively independent of total pressure. We did not find a good T-independent pressure indicator for these objects among the more abundant C-, N-, and O-bearing species investigated here.

The total pressure in the deep atmospheres of the more massive L and M dwarfs can be probed by the abundances of methyl (Fig. 11), HCN (Fig. 24) and HCNO (Fig. 26). Their abundances are relatively insensitive to the temperature at the expected P–T conditions for these hotter objects. A temperature indicator for M dwarfs is the abundance of CO_2 (Fig. 10). Finally, the abundances of NH are a potential temperature indicator for all types of objects with atmospheric conditions spanning the T and P ranges investigated here.

ACKNOWLEDGMENTS

Work supported by NAG5-6366 from the NASA Planetary Atmospheres Program (B.F.) and NSF AST-0086487 (K.L.). We thank Tristan Guillot for a detailed referee report and Mark Marley for comments.

REFERENCES

Anders, E., and N. Grevesse 1989. Abundances of the elements: Meteoritic and solar. *Geochim. Cosmochim. Acta* **53**, 197–214.

Barshay, S. S., and J. S. Lewis 1978. Chemical structure of the deep atmosphere of Jupiter. *Icarus* **33**, 593–611.

Bézard, B., H. Feuchtgruber, and Th. Encrenaz 1998. Detection of methyl radicals (CH_3) on Saturn. *Astron. Astrophys.* **334**, L41–L44.

Bézard, B., P. N. Romani, H. Feuchtgruber, and Th. Encrenaz 1999. Detection of the methyl radical on Neptune. *Astrophys. J.* **515**, 868–872.

Burgasser, A. J., J. D. Kirkpatrick, M. E. Brown, I. N. Reid, J. E. Gizis, C. C. Dahn, D. G. Monet, C. A. Beichman, J. Liebert, R. M. Cutri, and M. F. Skrutskie 1999. Discovery of four field methane (T-type) dwarfs with the two micron all-sky survey. *Astrophys. J.* **522**, L65–L68.

Burgasser, A. J., J. D. Kirkpartick, R. M. Cutri, H. McCallon, G. Kopan, J. E. Gizis, J. Liebert, I. N. Reid, M. E. Brown, D. G. Monet, C. C. Dahn, C. A. Beichman, and M. F. Skrutskie 2000a. Discovery of a brown dwarf companion to Gliese 570 ABC: A 2MASS T dwarf significantly cooler than Gliese 229B. *Astrophys. J.* **531**, L57–L60.

Burgasser, A. J., J. C. Wilson, J. D. Kirkpartick, M. F. Skrutskie, M. R. Colonno, A. T. Enos, J. D. Smith, C. P. Henderson, J. E. Gizis, M. E. Brown, and J. R. Houck 2000b. Discovery of a bright field methane (T-type) brown dwarf by 2MASS. *Astron. J.* **120**, 1100–1105.

Burrows, A., and C. M. Sharp 1999. Chemical equilibrium abundances in brown dwarf and extrasolar giant planet atmospheres. *Astrophys. J.* **512**, 843–863.

Burrows, A., M. S. Marley, and C. M. Sharp 2000. The near-infrared and optical spectra of methane dwarfs and brown dwarfs. *Astrophys. J.* **531**, 438–446.

Chase, M. W. 1999. NIST-JANAF thermochemical tables, 4th ed., *J. Phys. Chem. Ref. Data* **28**, Monograph No. 9, Am. Chem. Soc. and Amer. Inst. of Physics, Washington, DC.

Chase, M. W., Jr., C. A. Davies, J. R. Downey, Jr., D. J. Frurip, R. A. McDonald, and A. N. Syverud 1985. JANAF thermochemical tables, 3rd. ed., *J. Phys. Chem. Ref. Data* **14**, Suppl. 1, Am. Chem. Soc. and Amer. Inst. of Physics, Washington, DC.

Cuby, J. G., P. Saracco, A. F. Moorwood, S. d'Odorico, C. Lidman, F. Comeron, and J. Spyromilio 1999. Discovery of a faint field methane brown dwarf from ESO NTT and VLT observations. *Astron. Astrophys.* **349**, L41–L44.

Edvardsson, B., J. Andersen, B. Gustafsson, D. L. Lambert, P. E. Nissen, and J. Tomkin 1993. The chemical evolution of the galactic disk I. Analysis and results. *Astron. Astrophys.* **275**, 101–152.

Fegley, B., Jr., and K. Lodders 1994. Chemical models of the deep atmospheres of Jupiter and Saturn. *Icarus* **110**, 117–154.

Fegley, B., Jr., and K. Lodders 1996. Atmospheric chemistry of the brown dwarf Gliese 229B: Thermochemical equilibrium predictions. *Astrophys. J.* **472**, L37–L39.

Fegley, B., Jr., and H. Palme 1985. Evidence for oxidizing conditions in the solar nebula from Mo and W depletions in refractory inclusions in carbonaceous chondrites. *Earth Planet. Sci. Lett.* **72**, 311–326.

Fegley, B., Jr., and R. G. Prinn 1985. Equilibrium and non-equilibrium chemistry of Saturn's atmosphere: Implications for the observability of PH_3, N_2, CO, and GeH_4. *Astrophys. J.* **299**, 1067–1078.

Fegley, B., Jr., and R. G. Prinn 1986. Chemical models of the deep atmosphere of Uranus. *Astrophys. J.* **307**, 852–865.

Fegley, B., Jr., and R. G. Prinn 1988a. Chemical constraints on the water and total oxygen abundance in the deep atmosphere of Jupiter. *Astrophys. J.* **324**, 621–625.

Fegley, B., Jr., and R. G. Prinn 1988b. The predicted abundances of deuterium-bearing gases in the atmospheres of Jupiter and Saturn. *Astrophys. J.* **326**, 490–508.

Fegley, B., Jr., M. Yu. Zolotov, and K. Lodders 1997. The oxidation state of the lower atmosphere and surface of Venus. *Icarus* **125**, 416–439.

Gardiner, W. C. (ed.) 2000. *Gas-Phase Combustion Chemistry*. Springer-Verlag, New York.

Geballe, T. R., D. Saumon, S. K. Leggett, G. R. Knapp, M. S. Marley, and K. Lodders 2001. Infrared observations and modeling of one of the coolest T dwarfs, Gl 570 D. *Astrophys. J.* **556**, 373–379.

Griffith, C. A., and R. V. Yelle 1999. Disequilibrium in a brown dwarf's atmosphere: Carbon monoxide in Gliese 299B. *Astrophys. J.* **519**, L85–L88.

Guillot, T. 1999. A comparison of the interiors of Jupiter and Saturn. *Planet. Space. Sci.* **47**, 1183–1200.

Guillot, T., G. Chabrier, P. Morel, and D. Gautier 1994a. Nonadiabatic models of Jupiter and Saturn. *Icarus* **112**, 354–367.

Guillot, T., D. Gautier, G. Chabrier, and B. Mosser 1994b. Are the giant planets fully convective? *Icarus* **112**, 337–353.

Heirs, R. S., III 1994. Errors in JANAF thermodynamic formation functions for acetylene. *J. Thermophys. Heat Trans.* **8**, 181–182.

Kirkpatrick, J. D., I. N. Reid, J. Liebert, R. M. Cutri, B. Nelson, C. A. Beichmann, C. C. Dahn, D. G. Monet, J. E. Gizis, and M. F. Skrutskie 1999. Dwarfs cooler than "M": The definition of spectral type "L" using discoveries from the 2-Micron All-Sky Survey (2MASS). *Astrophys. J.* **519**, 802–833.

Lauretta, D. S., and K. Lodders 1997. The cosmochemical behavior of beryllium and boron. *Earth Planet. Sci. Lett.* **146**, 315–327.

Leggett, S. K., T. R. Geballe, X. Fan, D. P. Schneider, J. E. Gunn, R. H. Lupton, G. R. Knapp, M. A. Strauss, A. McDaniel, D. A. Golimowski, T. J. Henry, E. Peng, Z. I. Tsvetanov, A. Uomoto, W. Zheng, G. J. Hill, L. W. Ramsey, S. F. Anderson, J. A. Annis, N. A. Bahcall, J. Brinkmann, B. Chen, I. Csabai, M. Fukugita, G. S. Hennessy, R. B. Hindsley, Z. Ivezic, D. Q. Lamb, J. A. Munn, J. R. Pier, D. J. Schlegel, J. A. Smith, C. Stoughton, A. R. Thakar, and D. G. York 2000. The missing link: Early methane ("T") dwarfs in the Sloan Digital Sky Survey. *Astrophys. J.* **536**, L35–L38.

Lewis, J. S. 1969. Observability of spectroscopically active compounds in the atmosphere of Jupiter. *Icarus* **10**, 393–409.

Lewis, J. S., and R. G. Prinn 1980. Kinetic inhibition of CO and N_2 reduction in the solar nebula. *Astrophys. J.* **238**, 357–364.

Lewis, J. S., S. S. Barshay, and B. Noyes 1979. Primordial retention of carbon by the terrestrial planets. *Icarus* **37**, 190–206.

Lodders, K. 1999a. Alkali element chemistry in cool dwarf atmospheres. *Astrophys. J.* **519**, 793–801.

Lodders, K. 1999b. Revised thermochemical properties of phosphinidene (PH), phosphine (PH_3), phosphorus nitride (PN), and magnesium phosphate ($Mg_3P_2O_8$). *J. Phys. Chem. Ref. Data* **28**, 1705–1712.

Lodders, K. 1999c, Thermochemistry of atmospheres: From low-mass stars to Jupiter-like planets. In *Workshop Booklet and Scientific Program "From giant planets to cool stars*," p. 29. Northern Arizona University, Flagstaff, AZ.

Lodders, K., and B. Fegley, Jr. 1993. Actinide and lanthanide chemistry at high C/O ratios in the solar nebula. *Earth Planet. Sci. Lett.* **117**, 125–145.

Lodders, K., and B. Fegley, Jr. 1994. The origin of carbon monoxide in Neptune's atmosphere. *Icarus* **112**, 368–375.

Lodders, K., and B. Fegley, Jr. 1995. The origin of circumstellar SiC grains found in meteorites. *Meteoritics* **30**, 661–678.

Lodders, K., and B. Fegley, Jr. 1997a. Complementary trace element abundances in meteoritic SiC grains and carbon star atmospheres. *Astrophys. J.* **484**, L71–L74.

Lodders, K., and B. Fegley, Jr. 1997b. Condensation chemistry of carbon stars. In *Astrophysical Implications of the Laboratory Study of Presolar Materials* (T. J. Bernatowicz and E. Zinner, Eds.), pp. 391–423. AIP Conference Proceedings 402, American Institute of Physics, Woodbury, NY.

Lodders, K., and B. Fegley, Jr. 1998. *The Planetary Scientist's Companion,* Oxford Univ. Press, New York.

Lodders, K., and B. Fegley, Jr. 1999. Condensation chemistry of circumstellar grains. In *Asymptotic Giant Branch Stars* (T. Le Bertre, A. Lèbre, and C. Waelkens, Eds.), pp. 279–291. IAU Symposium No. 191, Astronomical Society of the Pacific, San Francisco, CA.

Mahaffy, P. R., H. B. Niemann, A. Alpert, S. K. Atreya, J. Demick, T. M. Donahue, D. N. Harpold, T. C. Owen 2000. Noble gas abundances and isotope ratios in the atmosphere of Jupiter from the Galileo Probe mass spectrometer. *J. Geophys. Res.* **105**, E15061–E15071.

Marley, M. S., D. Saumon, T. Guillot, R. S. Freedman, W. B. Hubbard, A. Burrows, and J. I. Lunine 1996. Atmospheric, evolutionary, and spectral models of the brown dwarf Gliese 229B. *Science* **272**, 1919–1921.

Martin, E. L., G. Basri, X. Delfosse, and T. Forveille 1997. Keck HIRES spectra of the brown dwarf DENIS-P J1228.2-1547. *Astron. Astrophys.* **327**, L29–L32.

Martin, E. L., X. Delfosse, G. Basri, B. Goldman, T. Forveille, and M. R. Zapatero Osorio 1999. Spectroscopic classification of late-M and L field dwarfs. *Astron. J.* **118**, 2466–2482.

Nakajima, T., B. R. Oppenheimer, S. R. Kulkarni, D. A. Golimowski, K. Matthews, and S. T. Durrance 1995. Discovery of a cool brown dwarf. *Nature* **378**, 463–465.

Niemann, H. B., S. K. Atreya, G. R. Carignan, T. M. Donahue, J. A. Haberman, D. N. Harpold, R. E. Hartle, D. M. Hunten, W. T. Kasprzak, P. R. Mahaffy, T. C. Owen, and S. H. Way 1998. The composition of the jovian atmosphere as determined by the Galileo probe mass spectrometer. *J. Geophys. Res.* **103**, 22831–22845.

Noll, K. S., T. R. Geballe, and M. S. Marley 1997. Detection of abundant carbon monoxide in the brown dwarf Gliese 229B. *Astrophys. J.* **489**, L87–L90.

Noll, K. S., T. R. Geballe, S. K. Leggett, and M. S. Marley 2000. The onset of methane in L dwarfs. *Astrophys. J.* **541**, L75–L78.

Oppenheimer, B. R., S. R. Kulkarni, K. Matthews, and T. Nakajima 1995. Infrared spectrum of the cool brown dwarf Gl 229B. *Science* **270**, 1478–1479.

Prinn, R. G., and S. S. Barshay 1977. Carbon monoxide on Jupiter and implications for atmospheric convection. *Science* **198**, 1031–1034.

Saumon, D., T. R. Geballe, S. K. Leggett, M. S. Marley, R. S. Freedman, K. Lodders, B. Fegley, and S. K. Sengupta 2000. Molecular abundances in the atmosphere of the T dwarf Gl 229B. *Astrophys. J.* **541**, 374–389.

Space Studies Board 1988. Space science in the twenty-first century. Imperatives for the decades 1995 to 2015. Overview, available at http://www.nas.edu/ssb/21och3.htm.

Space Studies Board 1991. Assessment of Solar System exploration programs 1991. 3 Exploration of the outer planets, available at http://www.nas.edu/ssb/ssep91ch3.htm.

Space Studies Board 1998. Failed stars and super planets. A report based on the January 1998 workshop on sub-stellar mass objects. Executive Summary, available at http://www.nas.edu/ssb/wsmoexecsum.htm.

Spilker, T. R., and W. B. Hubbard 1997. Science investigations from multiple deep (100 bar) Jupiter atmospheric entry probes. *Bull. Am. Astron. Soc.* **29**, 1019.

Strauss, M. A., and 28 colleagues 1999. The discovery of a field methane dwarf from Sloan digital sky survey commissioning data. *Astrophys. J.* **522**, L61–L64.

Stull, D., and H. Prophet 1967. The calculation of thermodynamic properties of materials over wide temperature ranges. In *The Characterization of High Temperature Vapors* (J. L. Margrave, Ed.), pp. 359–424. Wiley, New York.

Tsvetanov, Z. I., D. A. Golimowski, W. Zheng, T. R. Geballe, S. K. Leggett, H. C. Ford, A. F. Davidsen, A. Uomoto, X. Fan, G. R. Knapp, M. A. Strauss, J. Brinkmann, D. Q. Lamb, H. J. Newberg, R. Rechenmacher, D. P. Schnider, D. G. York, R. H. Lupton, J. R. Pier, J. Annis, I. Csabair, R. B. Hindsley, Z. Ivesic, J. A. Munn, A. R. Thakar, and P. Waddell 2000. The discovery of a second field methane brown dwarfs from Sloan Digital Sky Survey commissioning data. *Astrophys. J.* **531**, L61–L65.

Tsuji, T., K. Ohnaka, and W. Aoki 1996. Dust formation in stellar photospheres: A case of very low mass stars and a possible resolution on the effective temperature scale of M dwarfs. *Astron. Astrophys.* **305**, L1–L4.

Urey, H. C. 1953. Chemical evidence regarding the Earth's origin. In *XIIIth International Congress Pure and Applied Chemistry and Plenary Lecture*, pp. 188–217. Almqvist and Wiksells, Stockholm.

Yung, Y. L., W. A. Drew, J. P. Pinto, and R. R. Friendl 1988. Estimation of the reaction rate for the formation of methoxy radical from atomic hydrogen + formaldehyde: Implications for chemistry in the Solar System. *Icarus* **73**, 516–526.

Zolotov, M. Yu., and B. Fegley, Jr. 1998a. Volcanic production of sulfur monoxide (SO) on Io. *Icarus* **132**, 431–434.

Zolotov, M. Yu., and B. Fegley, Jr. 1998b. Volcanic origin of disulfur monoxide (S_2O) on Io. *Icarus* **133**, 293–297.